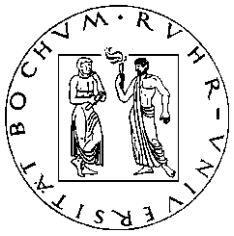

Optical Analysis of a Nanosecond Plasma Inside Liquids

Optische Analyse eines Nanosekundenplasmas in Flüssigkeiten

Bachelor Thesis

in the
degree program
“Bachelor of Science”
in Physics

at the Department of Physics and Astronomy
of the Ruhr-Universität Bochum

by

Maike Kai

from
Duisburg

Bochum 2018

Abstract

Plasmaentladungen in Flüssigkeiten bieten unter anderem Anwendungsmöglichkeiten in der Medizin, chemischen Synthese und der Wasseraufbereitung und sind daher Bestandteil der aktuellen Forschung. In Flüssigkeiten weisen Plasmaentladungen aufgrund der starken Produktion von freien Radikalen und Entstehung von Schockwellen eine hohe Reaktivität auf.
Das Entladungsverhalten von Plasmen in destilliertem Wasser, Ethanol und 0.9 % Natriumchloridlösung wird für 10 ns Spannungspulse bei Spannungen von 12 kV bis 30 kV und einer Frequenz von 1 Hz untersucht. Mittels Schatten- und Schlierenfotografie wird die Entladung abgebildet und die Bildung einer Schockwelle und ihre Geschwindigkeit untersucht.
Die Ausbreitung der Schockwelle ist ein zweistufiger Prozess. Während sich die Schockwelle während der ersten Phase mit supersonischer Geschwindigkeit bewegt, reduziert sich die Geschwindigkeit in der zweiten Phase zu der lokalen Schallgeschwindigkeit im Medium. Die aus den Geschwindigkeiten in destilliertem Wasser berechneten Drücke befinden sich im Bereich von 14 ± 4 GPa bis 45 ± 10 GPa während der ersten Phase und klingen zu Atmosphärendruck in der zweiten Phase ab.

Plasma discharges offer among others multiple applications in the field of medicine, chemical synthesis and water purification. This has made them an important object of current research. The high reactivity of discharges in liquids is closely connected to the production of radical species and formation of shockwaves.
The discharge behaviour of plasma discharges in distilled water, ethanol and 0.9 % sodium chloride is investigated for 10 ns voltage pulses between 12 kV and 30 kV at a frequency of 1 Hz. Shadowgraphy and schlieren imaging are used to visualise the discharge and analyse the formation of a shockwave and estimate its velocity.
The shockwaves' propagation has been found to be a two-staged process. During the first phase, the velocity of the shockwave is supersonic. It reduces to the local speed of sound in the medium during the second phase. The pressures in distilled water are calculated from the velocity and cover a range of 14 ± 4 GPa to 45 ± 10 GPa during the first phase and reduce to atmospheric pressure during the second phase.

Contents

1. Motivation

Plasma discharges in and in contact with liquids have become a major interest for the industry as they offer various applications in chemistry and biology [1] such as the destruction of microorganisms [2] and growth of nanoparticles [3]. The research on plasma-liquid interaction dates back more than 100 years as first studies on plasma discharges have been made in the late 19th century in the field of electrochemistry [4].

Nowadays, the number of possible applications of plasma-liquid interactions has grown. Over the past years, the use of plasma discharges in liquids in the environmental sector has become a focal point in this field of research [1]. Especially the application of these plasmas for water purification is in the main focus of these investigations. Therefor, additional solutions have to be identified to provide clean drinking water as conventional water treatment does not address all types of bacteria and toxins [5]. Furthermore, the water pollution in nature is increasing due to the intrusion of pesticides into the soil and groundwater [6] and disposal of wastewater containing textile dyes into rivers and open waters [7, 8].

Conventional water treatment includes ozone treatment, chlorine precursors and filtration [9]. Advanced oxidation processes (AOPs) are of particular interest when it comes to purifying water. These processes involve chemical reactions which aim to mineralise organic chemicals [10]. AOPs are defined as "chemical processes and precursors that have high reduction potentials and either produce OH or attack organic molecules directly" [5]. OH radicals are chief oxidisers which have the ability to mineralise organic compounds. Therefore, a high concentration of OH in water is needed. Sato, Ohgiyama, and Clements [2] have found that high concentrations of OH and H_2O_2 in water can be achieved by using pulsed high-voltage discharges. In addition, UV radiation, shock waves and further active radicals next to OH are produced by plasma discharges in liquids [11]. The treatment of water with plasmas could therefore be a future method for water purification and disinfection.

Further studies on the applications of discharges in fluids include chemical synthesis [12], material and medical applications [13] such as the synthesis of nanoparticles [14].

Discharges in different setups have been studied to gain a better understanding of plasma-liquid interaction [11, 15]. To this day, plasma-liquid interaction including the physics and the chemistry generated by the discharge has not been fully understood [15].

The plasma chemistry and surface reactions caused by the plasma treatment over the liquid phase are connected to receive information on the reactions between gas, liquid and solid phase. In this thesis, discharges for 10 ns pulses with voltage amplitudes of 12 kV to 30 kV are studied in a pin-to-pin setup.

While optical emission spectroscopy is used to gain information about the densities of various species such as oxygen, nitrogen and hydrogen, an optical analysis

like shadowgraphy or schlieren imaging gives information about the breakdown mechanism, formation of shockwaves and pressures inside the liquid. As the pressure inside the liquid influences the density of the species, both methods complement each other.

In the following, the plasma will be investigated optically. The stages of the discharge development inside distilled water, ethanol and sodium chloride are studied to gain a better understanding of the influence of different liquids' properties on the discharge behaviour. Additionally, the formation and propagation of a shockwave is analysed with regard to its temporal development and velocity. An estimation of the pressure is derived from the shockwaves' velocities to compare these to data gained from optical emission spectroscopy.
Voltage and current measurements are performed to estimate the dissipated energy into the discharge.

The knowledge of the discharge behaviour inside different liquids and the pressure values gained from the shockwave velocities contributes to the overall understanding of the discharge behaviour and the impact of the high pressures on the line broadening of the H_α line investigated by optical emission spectroscopy.

2. Theoretical Background

2.1 Characteristics of plasmas

The definition of a plasma is given by Chen [16] as "*a quasineutral gas of charged and neutral particles which exhibits collective behavior*".

Quasineutrality defines a state where a system seems uncharged to the outside. As a plasma consists of electrons, ions and neutral particles, this behaviour has to be defined more precisely. A measure of shielding of the plasma is given by the Debye length λ_D defined as

$$\lambda_D = \left(\frac{\epsilon_0 k T_e}{n e^2} \right)^{1/2} . \tag{2.1}$$

The permittivity is given by ϵ_0, k is the Boltzmann constant, T_e the temperature of electrons inside the plasma, n the density and e the charge of an electron.

If the dimension L of the plasma exceeds the Debye length, local changes in concentration of charged particles are shielded on a distance smaller than L. Therefore, the electron density n_e and ion density n_i are approximately equal. This quasineutrality is expressed by

$$L \gg \lambda_D. \tag{2.2}$$

The term "collective behaviour" expresses the dependence of the plasma's behaviour on conditions in local as well as remote regions [16].

To fulfil the requirements of collective behaviour, a minimum amount of particles in the plasma has to be given. To express this condition, the number of particles N_D in the "Debye sphere" is being defined as

$$N_D = \frac{4}{3} \pi n \lambda_D^3 . \tag{2.3}$$

To achieve collective behaviour, the number of particles in the Debye sphere must be greater than one.

$$N_D \gg 1 \tag{2.4}$$

Furthermore, a plasma-like behaviour is influenced by the frequency of plasma oscillations ω and the mean collision time τ between two neutral particles.

$$\omega \tau \gg 1 \tag{2.5}$$

If these three conditions are given, the fluid is in a plasma state.

A common breakdown mechanism is the Townsend breakdown which describes the breakdown mechanism based on electron avalanches. As free electrons in the vicinity of the cathode drift towards the anode, they may ionise the surrounding gas and cause electron avalanches. Townsend breakdown occurs at low pressures and short gaps for $pd < 4000\,\text{Torr cm}$ [17]. Free electrons have the ability to ionise atoms and molecules if their energy is sufficient for ionisation. In an electric field, electrons are accelerated in the direction of the field. The distance a particle can travel inside a medium before colliding with a second particle is called the mean free path between the particles. If the mean free path is large enough, electrons are able to gain enough energy to ionise other particle as they collide. If the number of free electrons rises rapidly due to ionisation, an electron avalanche takes place.

For larger gaps at high pressures, streamer or spark breakdown is the prevailing breakdown mechanism. Streamers are narrow channels filled by an ionised gas which propagate the path of a previous primary avalanche as this path is positively charged. The generation of photons caused by the avalanche induces secondary electron avalanches. The electrons travel along the trail of the initial electron avalanche and a streamer between the electrodes forms and luminous filamentary discharges occur [17, 18].

2.2 Plasma discharges in liquids

Discharges in liquids has been studied for several years, but there is still controversy about a precise description of the mechanisms causing the formation of a plasma inside liquids and about the influences of the experimental setup and liquid properties on the electrical breakdown, plasma ignition and propagation. In the following, an overview on the discharge setups and the discharge behaviour in liquids is given.

2.2.1 Discharge setups

Plasma-liquid interaction can be achieved by different setups. These can be divided into three main categories: Direct liquid phase discharges, discharge in gas phase with liquid electrodes and discharges in bubbles in liquids (fig. 2.2.1) [11].

Direct liquid phase discharge setups are characterised by two electrodes which are positioned inside the liquid. Commonly, plate-to-plate or plate-to-pin (fig. 2.2.1a) are used for non-thermal discharges.

If the liquid functions as an electrode and the anode is placed above the surface of the liquid, a setup for a discharge in the gas phase with a liquid electrode is used (fig. 2.2.1b). The discharge properties of discharges with a liquid electrode differ from metal electrodes due to the transport of charged particles and secondary emission coefficients.

The electrode configuration for discharges in bubbles in liquids is similar to the direct liquid phase discharge configuration. Powered and grounded electrodes

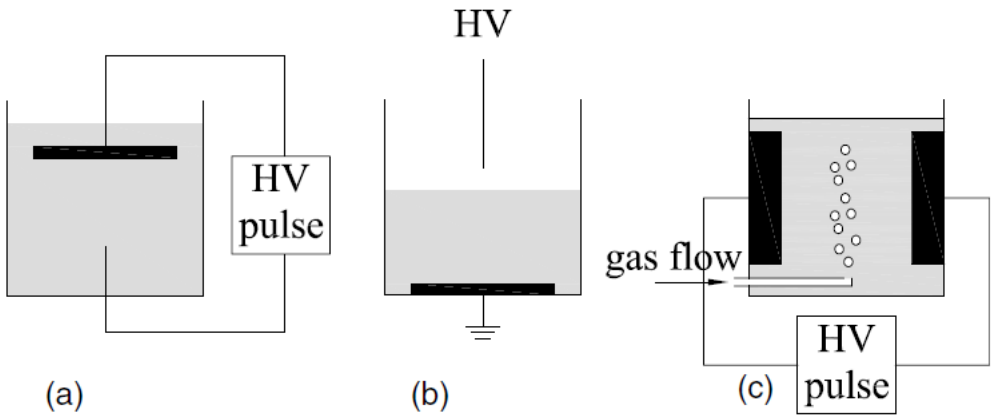

Figure 2.2.1: Electrode configurations for plasma discharges in and in contact with liquids. (a) direct liquid phase discharge reactor (b) gas phase discharge reactor with liquid electrode (c) bubble discharge reactor [11].

are placed inside the liquid. Additionally, a gas inlet is installed which produces bubbles inside the liquid (fig. 2.2.1c).

As a non-thermal direct liquid phase discharge will be investigated, the characteristics of discharges in these setups will be discussed in detail. For further information on plasma discharges in and in contact with liquids, Bruggeman and Leys [11] and Bruggeman et al. [15] have given an overview on the field of plasma-liquid interaction.

2.2.2 Discharge behaviour in liquids

Plasma formation in the liquid is characterised by the breakdown process which depends on the applied voltage, the shape of the pulse and the liquid properties [15]. Furthermore, material and shape of the electrode and the electrode configuration influence the formation of an electric field [19]. Electric field strengths of $1\,\mathrm{MV\,cm^{-1}}$ must be exceeded to enable streamer formation [20]. The electric field E is proportional to the effectively stressed electrode area A and the effective stress time t as following. The effective stress time is defined as the time the pulse is above 63 % of the maximum of the voltage pulse amplitude. The formula has originally been found for µs pulses but shows fairly good accuracy for voltage pulses applied at the cathode with a width of 10 ns or longer. For short voltage pulses applied at the anode, the dielectric strength exceeds the estimated by equation but the trend of the electric field is reflected.

$$E \propto A^{-n}\, t^{-1/3} \tag{2.6}$$

The constant n depends on the gap distance between the electrodes and the liquid properties [21, 22]. In addition, the pulse width τ influences the breakdown electric field in liquids [23]. All these factors must be considered when comparing plasma formation in liquids.

The breakdown phenomenon has to be examined to understand the process of

plasma formation in liquids. Electrical breakdown is defined as "the moment when a conductive plasma channel forms an electrical connection between the two metal electrodes inside the liquid" [11]. Several theories about the breakdown mechanisms in liquids have been discussed in literature [11, 22, 24, 25] as the electrical breakdown strongly depends on the experimental conditions [22].

Electric breakdown in liquids is believed to be caused by two separate mechanisms which are dependent on the voltage pulse [24, 25].
Direct ionisation has been observed by Starikovskiy et al. [26] for short high-voltage pulses. These pulses must have amplitudes of multiple kV and fast rise times as Joule heating occurs for longer pulses and electron acceleration can only occur at high voltages in dense media. While high electric fields in comparison to the plasma ignition in air are needed for breakdown in liquids [11], the reduced field strength E/n is important for the breakdown in liquids. The reduced field strength is the ratio between the electric field E and the particle density n in the medium and therefore a value for the impact of the electric field on the particles. As the density in gases is much lower than the density of liquids, breakdown fields in liquids are higher than those in gases [24]. Therefore, discharges in the gas phase are more common. Ionisation in the gas phase is therefore described by the steam-gas mechanism. This mechanism includes several phenomena like gas bubbles, cavitation and electrothermal mechanisms [24].

Tereshonok et al. [24] describe the breakdown process in gas-liquid systems as a four-stage process. During the first stage of the order of 1 ns, fast processes take place. These processes include the formation of cavitation voids, Townsend breakdown and streamer breakdown.
The second stage covers 100 ns after the voltage has been applied. During this stage, liquid vapour fills the cavitation bubbles.
On a timescale in the magnitude of 10 µs to 30 µs breakdown phenomena occur. The streamer-leader breakdown is found to be the leading breakdown phenomenon. While breakdown due to Townsend mechanism is the main breakdown cause for $pd < 200$ Torr cm, streamer-leader is predominant for $pd > 4000$ Torr cm. The non-uniform electric field in the area surrounding the electrode reaches its maximum strength in the vicinity of the electrode tip. If the local electric field is sufficient for a transition from avalanche to streamer, a plasma channel is formed. This plasma channel is charged itself and has a high electric field strength at its tip. The propagation of the channel depends on the external electric field and the channel expands with rising field strengths [27].
The fourth stage is characterised by slow processes such as thermal breakdown processes which evolve on timescales up to several µs.

The plasma emission is linked to the temporal change of the applied voltage. At the rising edge of the voltage pulse, dV/dt is greater than zero and the emitting regions grows. During the voltage plateau, there is no temporal change of the voltage. During this dark phase there is no plasma visible. The plasma ignites at the falling edge of the voltage pulse again, as dV/dt does not equal zero [28]. This corresponds to the above-mentioned interdependence of channel propagation and external electric field.

2.3 Non-uniformities in the liquid phase

During the different stages of the plasma evolution, several different non-uniformities form inside the liquid. These phenomena are spread on a scale between nanometres and millimetres.

2.3.1 Formation of voids and nanopores

The formation of voids and nanopores occurs directly after the application of the voltage pulse. At the rising edge of the voltage pulse, a large negative pressure forms inside the fluid for voltage pulses with short rise times and these pulses create inhomogeneous electric fields. Electrostriction forces in the electric field cause the dielectric liquid to move towards the highest field strength. Due to these effects, irregularities occur in the vicinity of the electrode tip. The occurrence of these irregularities can been found under the term of the formation of nanopores, cavitation or voids in the liquid in literature. In contrary to gas bubbles, the above explained irregularities are not of a gaseous nature [25, 29].

The formation of voids and nanopores enables breakdown in the liquid phase as electrons are able to gain energy through acceleration inside the voids. If the pathway is long enough, the electrons reach an energy sufficient for ionisation and cause electron multiplication. Therefore, the formation of voids and nanopores enhances electron avalanches which can initiate electric breakdown [28].

2.3.2 Streamer and bubble formation

Ruptures inside liquids forming pathways between the electrodes are called streamers or channels [22]. Streamers commonly refer to luminous filamentary discharges while channels are gaseous ruptures in the liquid which remain after the formation of streamers in the liquid. Channels do not have to be luminous but can be distinguished from the surrounding liquid due to their optical properties. The difference can be observed as the channels have a different refractive index than the medium [22]. The nature of the streamers has not been identified yet. Streamers could either be of gaseous nature [22, 30] or ruptures in the liquid which have a lower density than the surrounding liquid [22, 31]. In literature, channel and streamer are often used as synonyms but will be distinguished by the above given definition in the following.

Streamer initiation is caused by electron avalanches. Its propagation depends on the applied voltage pulse and electric field, the liquid properties and surrounding pressure. Two different types of streamers appear depending on the applied voltage. For low voltages, primary streamers propagate at subsonic speed. Primary streamers have a bushlike shape and are field-dependent. For high voltages, secondary streamers with a filamentary or tree-like structure evolve. The propagation of secondary streamers is mainly independent of the electric field. While the applied voltage has no significant influence on the streamer velocity, it affects the number of streamer branches. Secondary streamers propagate at su-

personic speed [20]. Marinov et al. [32] have found that while bush-like streamers propagate at a few $\mathrm{km\,s^{-1}}$ and their formation is not dependent on the formation of cavities in the liquid, tree-like streamers travel at $10\,\mathrm{km\,s^{-1}}$ to $100\,\mathrm{km\,s^{-1}}$.

A spherical gaseous cavity, often called bubble, forms at the tip of the electrode after the applied voltage pulse for low voltages and during the plateau of the voltage pulse for high voltages. The cavity grows slowly at subsonic speed. Due to the hydrodynamic pressure on the spherical cavity, it only increases to a limited radius and collapses. During its growth, the radius of the bubble oscillates due to the pressure imbalance [33].

2.3.3 Shockwaves and pressure waves

The terms shockwave and pressure wave are commonly used as synonyms but are defined differently. While pressure waves are of subsonic or sonic nature, shockwaves are caused by fast pressure changes inside a medium and move at supersonic speed. A cause for shockwaves are impacts in the liquid at a high velocity [34].

Several theories about the formation of a shockwave after a plasma discharge inside liquids have been established. An, Baumung, and Bluhm state that streamer development causes the formation of compression waves around the streamer. The formation of a pressure field is directly linked to the channel expansion.

Seepersad et al. [28] have found that a region of cavitation in the vicinity of the electrode tip is associated with a negative pressure in this area. The formation of this area is faster than the formation of hydrodynamic forces. Therefore, the reaction of the hydrodynamic forces on the negative pressure is delayed. As the hydrodynamic forces set in, they push towards the electrode. This leads to the formation of a compression layer. When the negative pressure decreases, the compression layer relaxes and travels away from the electrode.

The negative pressure in the vicinity depends on the applied electric field as the force $\vec{F}$ acting on a polar fluid depends on the electric field E as

$$\vec{F} \approx \frac{\alpha \epsilon \epsilon_0}{2} \vec{\nabla} E^2 \,. \tag{2.7}$$

α is a characteristic constant for the liquid and ϵ the permittivity of the liquid.

As the electric field is dependent on the applied voltage, the amplitude of the negative pressure rises with increasing voltage pulse amplitudes [28, 35].

3. Experimental setup

In the following section, the experimental setup will be described with special regard to the power system including voltage and current measurements and a shadowgraphy and schlieren imaging setup for an optical analysis of the plasma.

3.1 Discharge chamber

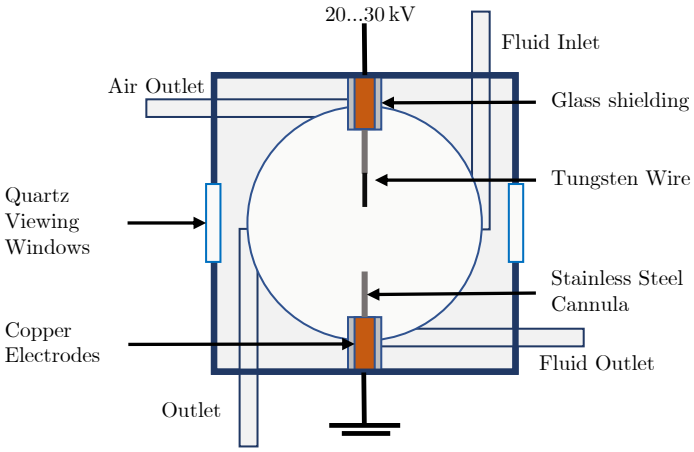

Figure 3.1.1: Discharge chamber with a pin to pin setup.

The plasma is ignited inside a chamber made of PMMA with a pin-to-pin setup with a volumetric capacity of 25 ml (fig. 3.1.1). The copper electrodes are shielded by a glass tube and connected to a cannula made of stainless steel. The top electrode is connected to the power generator. To reach sufficient field strengths, a tungsten wire is mounted inside the cannula. The bottom electrode is grounded. The distance between the tungsten wire and the bottom cannula is 3 mm to 8 mm.

Two different tungsten wires (fig. 3.1.2) are used. The first wire is a 50 µm wire (fig. 3.1.2a). During the measurements, the 50 µm wire was exchanged several times due to signs of wear. Therefore, the form of the tip may slightly vary from the wire shown. The second wire is approximately 387 µm in diameter. Its tip was sharpened mechanically to enable higher field strengths. The shape of the tip is depicted in figure 3.1.2b. The images were taken with a Color 3D Laser Microscope by Keyence.

The inlet is positioned on the upper side of the chamber, the outlet for the liquid is situated at the bottom. A third outlet for air is positioned at the side of the chamber. The windows of the chamber are made of quartz glass.

Distilled water, pure ethanol and 0.9 % sodium chloride are used as liquids inside the chamber. The sodium chloride solution consists of 9 g sodium chloride in 1 l

of distilled water.

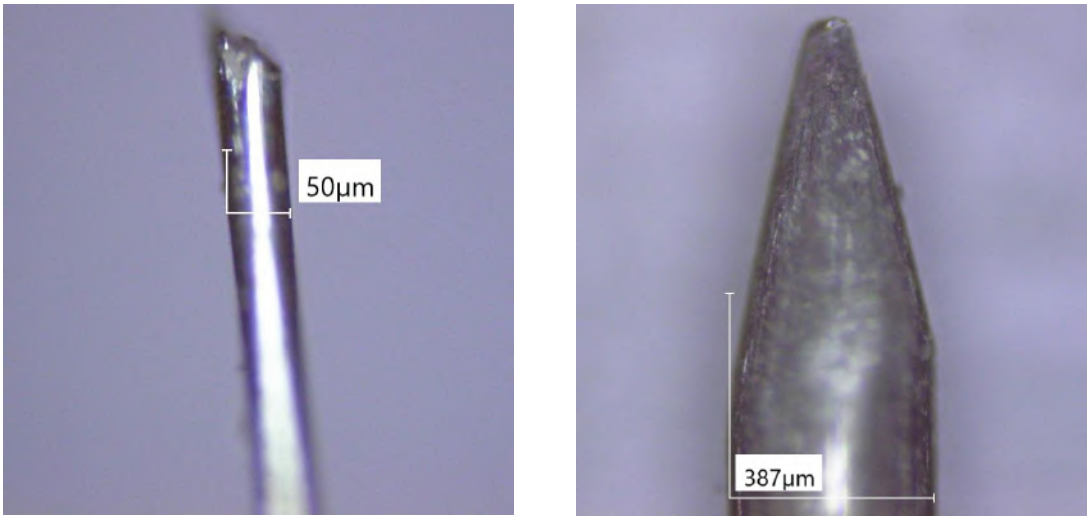

(a) 50 µm tungsten wire (b) 387 µm tungsten wire

Figure 3.1.2: Images of tungsten wires used for shadowgraphy and schlieren imaging taken with a laser microscope

3.2 Power supply system

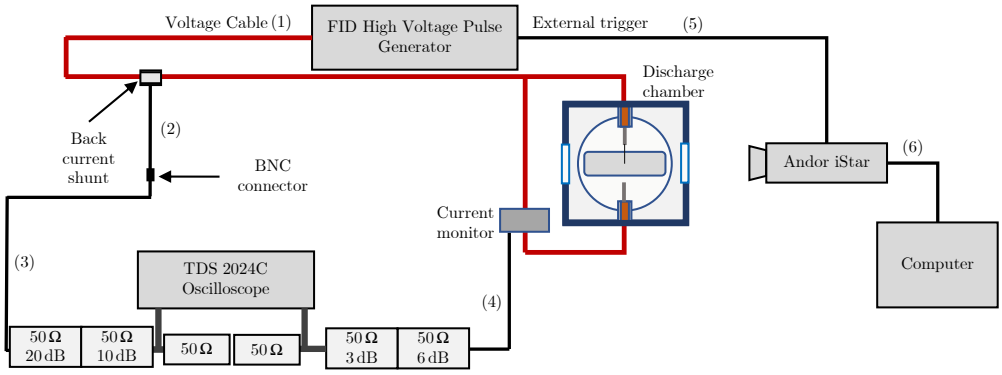

Figure 3.2.1: Experimental setup with electric circuit. All cables are labled with numbers, the lengths are listed in table 3.1.

The electric circuit is pictured in figure 3.2.1. The power is provided by an FPG 30-01NK10 High Voltage Pulse Generator by FID GmbH which provides voltages in the range of 10 kV to 30 kV powered at frequencies between 1 Hz and 100 Hz with pulse rise times of 2 ns to 4 ns. A RG217 coaxial cable made of copper connects the power generator to the electrodes. The inner conductor provides the voltage, the outer conductor is grounded. The power cable is connected to the electrodes in the chamber (fig. 3.1.1).

Two different cables are used which are both of the same type. The short cable is made of one single cable. The longer cable is made of two short RG217 cables. The cables' characteristic wave impedance is 50 Ω. A back current shunt (BCS) consisting of eleven parallel 3.3 Ω resistors which equals a joint resistance of 0.33 Ω, is mounted on the outer conductor to measure the incoming voltage. The back current shunt cable can be connected to a BNC cable for voltage measurements. The construction of the shunt follows the setup described in [28].

A Pearson Electronics Inc 8590C Current Monitor is placed around the cable of the grounded electrode and connected to the oscilloscope with a BNC cable. The BNC cable for voltage measurements connects the shunt to the oscilloscope. The details of the voltage measurement are described in section 3.2.2 and the current measurement in section 3.2.3.

The Andor iStar camera used for an optical analysis of the plasma is connected to the external trigger of the pulse generator. The camera is connected to a computer to record the signal. The internal delay of the camera is 45 ± 2 ns.

All cables are shielded with magnetic cores to minimise disturbances due to electromagnetic interference.

The cables' characteristics are listed in table 3.1. The voltage cable with a length of 3.40 m was used for shadowgraphy which will be referred to as setup 1 in the following. The cable with a length of 9.12 m was used in setup 2 for schlieren imaging.

Table 3.1: Cable lengths and distances in setups 1 and 2. Numbers of cables match labels in figure 3.2.1.

		cable length / m	
		#1	#2
(1)	voltage cable	3.40	9.12
	BCS to pulsed electrode	0.96	7.32
	BCS to grounded electrode	0.85	7.34
(2)	BNC cable of BCS	1.48	0.46
(3)	BNC connector of BCS to oscilloscope	3.58	
(4)	current monitor to oscilloscope	3.04	
(5)	camera trigger cable	2.58	
(6)	camera cable to computer	3.09	
	uninsulated cable at oscilloscope	4.94	

3.2.1 Calculation of delay

To match the measurements of setup 1 and 2, the delay t_{delay} caused by the cables and camera needs to be calculated. A velocity of $3\,\mathrm{ns\,m^{-1}}$ is assumed to be the speed of the signal inside the cables for an estimation of the delay times. The exact speed of the signal inside the cable is unclear, as estimations of the signal velocity from measurements of temporal distance initial voltage pulse and reflected pulses for different cable lengths (fig. 3.2.2 and 3.2.3a) result in different values. For the short cable, the pulses have a distance of 14.27 ns which corre-

sponds to a velocity of 2.1 ns m^{-1} inside the cables. The pulses have a separation of 70.986 ns using the long voltage cable which corresponds with a signal velocity of 3.9 ns m^{-1}. As the velocity of the signal inside the short cable would be higher than the speed of light, there must be an error in the estimation of the temporal difference between the pulses. As both values are close to the speed of light, this value is assumed to be a sufficient guiding value.

The delay is calculated by

$$t_{delay} = l_{total} \cdot v_{sig} \, . \tag{3.1}$$

The total cable length between pulse generator and measuring device is l_{total} and the speed of the signal is v_{sig}. The individual cable lengths are listed in table 3.1.

The delays between the power generator and measuring devices are listed in table 3.2.

Table 3.2: Delays between power generator and measuring devices in setups 1 and 2

	delay / ns	
measuring device	#1	#2
Plasma:	/	/
initial pulse	10.2	27.36
pulse reflected at pulser	30.6	82.08
Camera:	52.74	52.74
Oscilloscope:		
Initial voltage pulse	22.5	17.52
Pulse reflected at plasma	28.26	61.44
Pulse reflected at pulser	42.9	72.24
Current	9.12	9.12
Interfering signal	14.82	14.82

3.2.2 Voltage measurement

The shunt is connected to a Tectronix TDS 2024C oscilloscope. The oscilloscope has an input impedance of 1 MΩ. Magnetic cores are placed around the cable near the connection to the oscilloscope to avoid the impact of electromagnetic interference on the measurements. Two 50 Ω resistors with a reduction of 10 dB and 20 dB are installed between the cable and the oscilloscope to adapt the voltage signal to the measurement range of the oscilloscope. A third resistor of 50 Ω is attached to the end of the cable on a T-piece (fig. 3.2.1).

A cable with an uninsulated end was connected to the same resistors used for the voltage measurements to estimate the influence of electromagnetic interference on the signal measured over the back current shunt. The uninsulated end was mounted outside the chamber close to the tip of the wire.

The voltage and current in the cable are calculated according to Seepersad et al. [28].

$$I^{+}(z,t) = \frac{Z_{out} + Z_{scope}}{Z_{scope}} \frac{V_{scope}}{Z_{shunt}} \cdot \gamma \tag{3.2}$$

The line current $I^{+}(z,t)$ depends on the position in the cable z and time t. It can be calculated from the impedance Z_{out} of the shunt connector and Z_{scope} of the oscilloscope. The voltage V_{scope} is measured by the oscilloscope. As resistors attenuate the incoming signal in the oscilloscope, the attenuation is expressed by the factor γ.

As the impedance of the shunt connector is 50 Ω, it is remarkably smaller than the 1 MΩ impedance of the oscilloscope. Accordingly, equation 3.2 can be expressed in a simplified equation. γ is $10^{1.5}$ for a total attenuation of 30 dB consisting of a 10 dB and 20 dB attenuation for the voltage measurement at the back current shunt. For a total attenuation of 9 dB used for the current measurement, the attenuation factor changes to $10^{9/20}$.

The line current at the back current shunt is estimated by equation 3.3 for a total attenuation of 30 dB. For an attenuation of 9 dB, equation 3.2 simplifies to equation 3.4.

$$I^{+}_{30\,dB}(z,t) = 105.41 \cdot V_{scope} \tag{3.3}$$

$$I^{+}_{9\,dB}(z,t) = 9.39 \cdot V_{scope} \tag{3.4}$$

As the voltage signal is not only levelled down by the attenuators but also by the 50 Ω impedance of the cable, the amplitude of the voltage measured by the oscilloscope is adjusted by the factor 50 as

$$V^{+}(z,t) = 50 \cdot I^{+}(z,t)\ . \tag{3.5}$$

A voltage pulse at 20 kV and 1 Hz in setup 1 is shown in figure 3.2.2. The start point of the voltage pulse is set as zero on the time axis. The rising front has a duration of 3 ns and reaches a maximum strength of 22 kV. Following, the pulse reaches a plateau at 15 kV for 5 ns and falls back to zero for 2 ns. In addition to the initial pulse, the pulse reflected at the plasma and the pulse reflected at the power generator are shown. The reflected pulse which reaches a maximum amplitude of 20.5 kV.

Voltage measurements at different temporal resolutions for setup 2 are shown in figure 3.2.3. All pulses have been recorded with 64 accumulations. The timescale is adapted to the beginning of the rising front of the voltage pulse. As electromagnetic interference is strongly present and could not be completely prevented by shielding the setup with a Faraday cage of stainless steel and the cables with magnetic cores, the form of the voltage pulse has to be estimated from the disturbed measurements. Both figures 3.2.3a and 3.2.3a show voltage signal captured by the back current shunt and the signal captured by the uninsulated cable.

In figure 3.2.3a, the initial pulse and its reflection at the plasma are shown in detail. A first peak of a magnitude of 15 kV occurs during the 5 ns before the initial

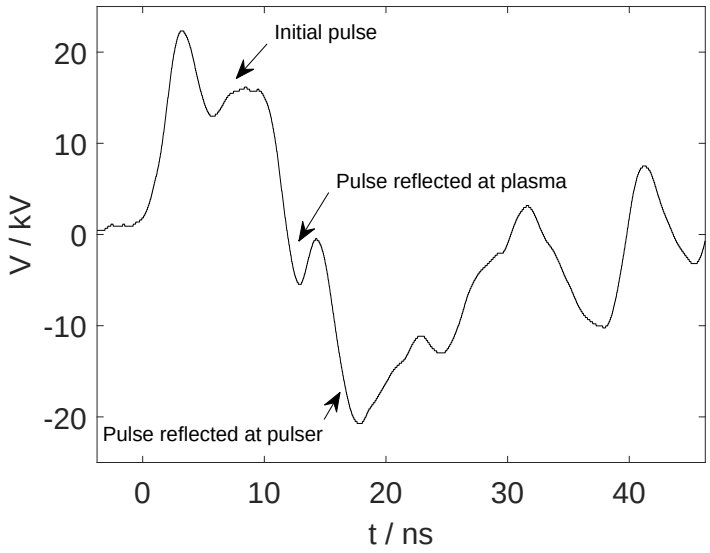

Figure 3.2.2: Voltage measurements at 1 Hz of 20 kV pulse recorded with 16 accumulations in setup 1.

voltage pulse. This peak is probably caused by electromagnetic interference, as the peak can also be clearly seen in the interfering signal recorded by the uninsulated cable. The voltage pulse starts at 0 ns and has a duration of 10 ns. The duration of the rising front can only be estimated to 1 ns, as the first peak could overlap with the voltage pulse and cut of the first few nanoseconds of the rising edge. After the rising edge, a plateau forms and last for 4 ns before the voltage decreases. The falling edge of the pulse lasts for 5 ns. The plateau of the voltage pulse is at 4 kV for an amplitude of 10 kV.

The voltage measurements over a time period of 250 ns is plotted in figure 3.2.3b.

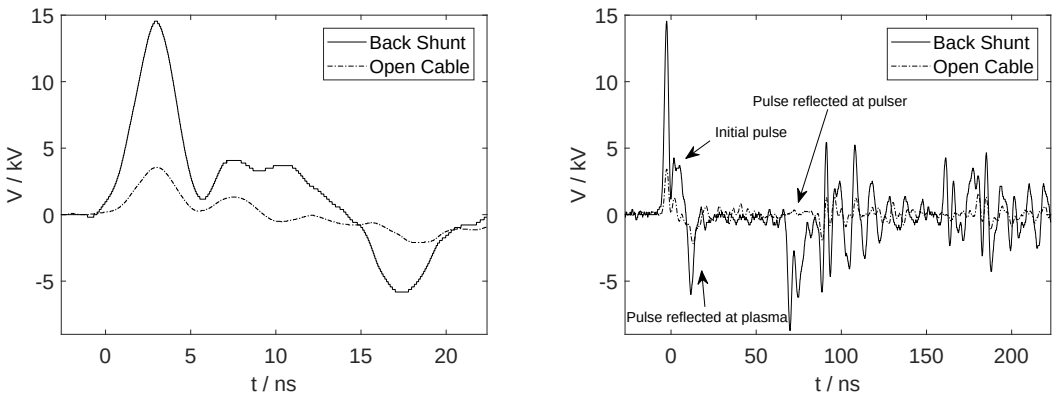

(a) Detailed measurement of initial voltage pulse.

(b) Voltage measurement over time period of 250 ns

Figure 3.2.3: Voltage pulse and interfering signal of setup 2 recorded for generator power of 10 kV and 1 Hz with 64 accumulations. Time axis shifted to start of rising front of voltage pulse.

The initial pulse occurs during the first 10 ns and is directly followed by a negative pulse which occurs due to the partial reflection of the pulse at the plasma. A third pulse is recorded at 65 ns after the first pulse. This pulse is caused by the reflection of the voltage pulse at the power generator. The following peaks are caused by electromagnetic interference and oscillations in the cable but do not represent a voltage input into the plasma.

3.2.3 Current measurement

The current monitor is placed around the cable of the shunt to measure the current in the outer conductor. The monitor measures currents at $1\,\mathrm{A\,V^{-1}}$. Two $50\,\Omega$ resistors with a reduction of 3 dB and 6 dB are installed between oscilloscope and the cable leading from the current monitor with a third $50\,\Omega$ resistor at the end of the T-piece. All currents are measured with 64 accumulations.

The possibility of an influence of a magnetic field generated by the current on the voltage cable was excluded by measuring the magnetic field near the cage with a Gaussmetre. No change to the magnetic field near the cage could be observed after the pulse generator was turned on.

Measurements of the current show a strong influence of disturbance though. To reduce the interference, the pulse generator is operated at pre-breakdown voltage of 10 kV and 1 Hz. The stainless steel cannula and tungsten wire are removed from the top electrode. Therefore, the current flow should be close to zero. Measurements show a strong discrepancy though (fig. 3.2.4a). The current signal has an oscillating behaviour with an exponential decline. An interfering signal measures by an uninsulated cable connected to the attenuators which were used for the current measurements could not be matched to the current measurement.

Reference measurements over a 10 dB and 20 dB attenuator show that the shape of the current pulse at a voltage of 10 kV stays constant (fig. 3.2.4b).

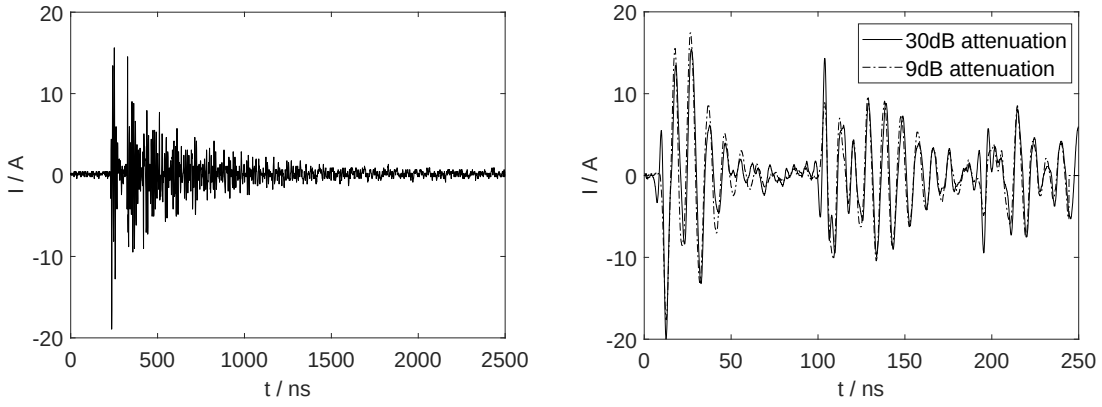

(a) Full current signal.

(b) Comparison of current measurement at a total attenuation of 9 dB and 30 dB.

Figure 3.2.4: Current without plasma ignition measured at 10 kV and 1 Hz with 64 accumulations .

3.3 Conductivity measurements

The electric conductivity of the fluids is measured before and after the plasma treatment of the fluid. Treatment periods between 5 min and 45 min have been examined. A GLF100 by GHM Messtechnik was used. Significant changes in the conductivity caused by the plasma treatment could not be observed. The conductivity of distilled water is approximately 2 µS cm^{-1}, of ethanol 6 µS cm^{-1}, and of 0.9 % Sodium Chloride 1.4 mS cm^{-1}.

3.4 Optical analysis

Shadowgraphy and schlieren technique are used to analyse the plasma optically.

Shadowgraphy technique is used to picture disturbances and non-uniformities in the liquid. The refractive index of a medium is greatly influenced by the number of particles per volume and to a small extent by the species in the medium. Due to refractive index gradients inside the fluid with density gradients, light rays are deflected differently along the gradient [36]. This causes areas of different intensities on the screen.

Schlieren imaging is used to depict refractive index perturbations as contrast changes and to derive information about density perturbations in the fluid [25].

3.4.1 Shadowgraphy

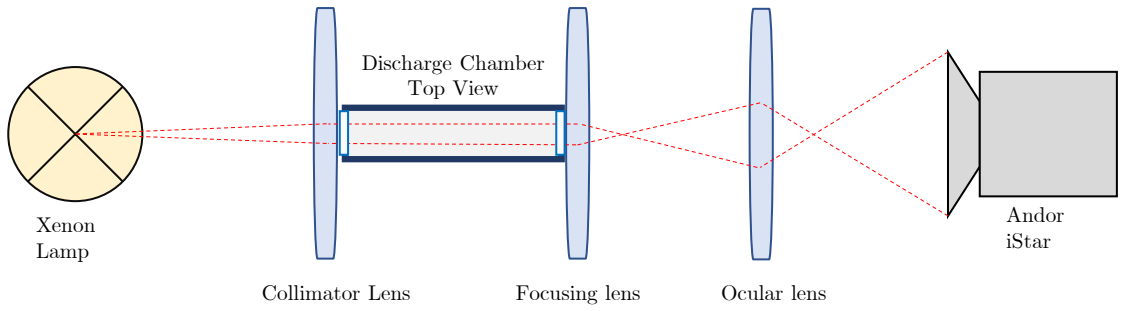

Figure 3.4.1: Shadowgraphy setup consisting of a xenon lamp, collimator lens, discharge chamber, focusing lens, ocular lens and camera.

A setup consisting of lenses is used to produce a large image of the plasma (fig. 3.4.1). A Xenon lamp LXH 100 by Müller Elektronik-Optik is used as the light source. The intensity distribution of the lamp is adapted by an internal lens and set to a uniform intensity along the image. The light rays are aligned with a collimator lens with a focal length of 100 mm to create parallel light rays which travel through the discharge chamber. In the discharge chamber, a 50 µm tungsten wire is used to create large field strengths needed for an ignition of the plasma.

A focusing lens with a focal length of 30 mm produces a shadowgraph image. An ocular lens with a focal length of 20 mm is placed behind the focusing lens to turn and enlarge the image. The image is recorded by a Andor iStar camera with a 1024x1024 CCD chip inside.

The image is converted into an ASCII-file and then into an image for the analysis. The calibration factor is determined from the width of the 50 µm wire. The width of the wire in pixels is identified as an average width of the wire in 20 images. Due to a slight blur of the image, the error of the pixel width was set as the read-out inaccuracy instead of the standard deviation of the pixel widths to include the constant error of the blur of the wire. Due to the converting process of the image, the output image of the ASCII file is a 828 pixel x 828 pixel image. The shockwave velocity is estimated from these images with a calibration factor of $4.3 \pm 1.6\,\mu\text{m}\,\text{pixel}^{-1}$. For other image sizes, the calibration factor was adapted to the scale of the image.

3.4.2 Schlieren imaging

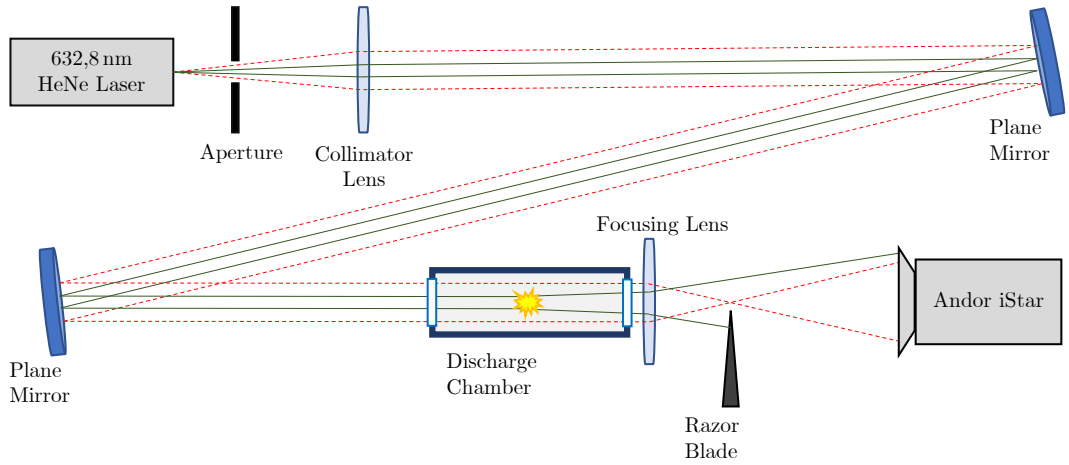

Figure 3.4.2: Schlieren setup consisting of a HeNe laser, aperture, collimator lens, plane mirrors, a discharge chamber, focusing lens, razor blade and camera.

Schlieren images can be achieved using various setups. An overview is given in [37]. A z-type setup is chosen to obtain a sharp image and larger illuminated area (fig. 3.4.2).

The light source is a Spindler & Hoyer HeNe 633-2sp laser operating at a wavelength of 632.8 nm and a power of 5 mW. The Xenon lamp is not suitable for schlieren imaging as the intensity loss due to the optical components is too great.

As the laser beam is not perfectly parallel and interferences occur, an aperture is used behind the laser. The size of the opening of the aperture is adapted to the main maximum of the interference pattern. Only the light beam of the main maximum passes the aperture. A collimator lens with a focal length of 100 mm creates a single parallel beam which is reflected by two plane mirrors positioned

on opposite sides with a maximum distance in between to increase the travel path of the beam. This increase optimises the diameter of the light beam as it expands over a large distance.

The mirrors are aligned in an angle which focuses the beam on the tip of the tungsten wire. A 387 µm wire is used to avoid movement of the wire as the 387 µm wire is more rigid than the 50 µm wire. The tip of the wire was mechanically sharpened to enable high field strengths required for igniting the plasma.

A focusing lens with a focal length of 30 mm behind the discharge chamber focuses the light beam on a horizontally oriented sharp razor blade. Density perturbations in fluids cause changes in the local refractive index. As the deflection of light beams depends on the refraction index of the medium, beams that have passed the plasma influenced regions in the fluid are deflected differently. Therefore, the light is partly absorbed by the razor blade and only a fraction of the light beam reaches the Andor iStar camera. An image with lighter and darker regions is created on the CCD of the camera. Areas with different intensity correspond with different refractive indices.

The calibration of the image is achieved by determining the number of pixels for a 610 µm ceramic tube instead of the tungsten wire to improve the accuracy of the calibration. As the ratio of the width of the wire in pixels to the read-off inaccuracy of the edge of the pipe increases, the error of the calibration factor decreases. For an 828 pixel x 828 pixel image, the calibration factor was determined to $1.91 \pm 0.24\,\mu\text{m}\,\text{pixel}^{-1}$.

4. Results

In this section, the results of the measurements are outlined and discussed. Furthermore, the findings are compared to results of other research groups with similar experimental setups.

The challenges which arose during the process are discussed and solutions are presented.

4.1 Voltage and current measurements

The voltage pulse generated by the power supply has a great influence on the characteristics of the plasma discharge due to the pulses short rise time, as pointed out in section 2.2.2. Therefore, a knowledge of the shape of the voltage pulse is of great interest.
The occurrence of electromagnetic interference caused by nanosecond voltage pulses with short rise times is a common phenomenon.

Setup 1 was used during the first experiments. While there were no disturbances due to electromagnetic interference during the measurements in water and ethanol, weak disturbance of the computer occurred during the measurements of sodium chloride. Due to a defect of the cable which could not be precisely located, a high amount of high frequency interference was generated during the construction of the schlieren setup. As weak spots, the connection to the pulse generator, the back current shunt and the electrode joints were determined. The electromagnetic interference disturbed the camera and its trigger. Furthermore, voltage measurements show strong oscillations. Light emission of high frequency interference cannot be avoided but its effects are minimised by shielding the experimental setup with a grounded cage and using magnetic cores. The amount of interference generated by the defect of the cable could not be reduced sufficiently.

The cable was exchanged to the 9.12 m high voltage cable to guarantee precise functioning of the camera. Due to its length, the delay of the initial voltage pulse and the pulse reflected at the pulse generator are shifted. Additionally, the shape of the voltage pulse differs from the pulse of the short cable. It is likely that this difference is caused by the structure of the cables. While the short cable is made of one piece, two short cable are soldered for the long cable. The solder joint is a weak spot of the cable, as the formation of electromagnetic interference is facilitated. This increased occurrence of interference is a probable cause for the varying shapes of the initial voltage pulse.

The measurements with an open cable show the strong occurrence of electromagnetic interference (fig. 3.2.3). As this phenomenon could not be solved using magnetic cores either, currents and voltages were measured at pre-breakdown voltage without a tungsten wire as electrode to minimise the amount of interference. The oscilloscope placed outside the cage and was connected to a different

power point than the pulse generator to separate the electric circuits and eliminate interference transported via the power cable.

Current measurements were attempted for setup 2 to get a better impression of the discharge characteristics and estimate the dissipated energy (fig. 3.2.4). As the problem of interference described above also occurred for these measurements, currents were detected at pre-breakdown voltage. Therefore, current measurements could not be executed as the current signal could not be matched to the voltage signal. Further restrictions of the current measurements are caused by the current monitor. As it is mounted around the cable of the grounded electrode, it is located inside the cage and it exposed to a high level of electromagnetic interference. Additionally, the current cable needs to be placed in a centred position leading through the current monitor. The positioning of the cable is limited due to its short length. Due to the size of the current monitor, it can only be positioned around a short part of the cable. These restrictions limit the alignment of the current monitor and inhibit a precise setup of the current measurement.

Multiple measurements of the current show the persistence of the disturbance. Since the signal is recorded without a tungsten wire and at pre-breakdown voltage, it is not suitable as background subtraction as every change of the setup and voltage causes a change in the voltage and current signal. Therefore, a measurement of the voltage pulse for breakdown voltages with plasma ignition could not be executed because no disturbance signal could be recorded as background subtraction on the current and voltage measuring cable. The amplitude of the interference captured by the open cable is not sufficient to be used as background subtraction.

The energy which was dissipated into the plasma can be estimated from measurements of the current at the grounded electrode and an analysis of the development of the current, such as measurements of the amplitude of the voltage pulse. As the current measurements are strongly disturbed by electromagnetic interference, the first method cannot be applied to these measurements. As the measured currents are not single peaks but an oscillating pattern, no statements on the current caused by the plasma and its temporal development can be made as the current signal cannot be matched to the voltage pulses. An alternative method estimates the dissipated energy from a comparison of the initial voltage pulse and the reflected voltage pulses [27]. As the voltage measurements are influenced strongly by electromagnetic interference as well and the position of the pulses have no clearly defined beginning and end, an estimation of the dissipated energy cannot be performed.

A voltage cable made out of one single piece should be used to decrease the weak spots of the cable and improve the voltage and current measurement. Furthermore, a large cable length is advisable to have a clear separation of initial and reflected pulse and allow precise positioning of measurement devices. Further shielding of the cables and measuring devices need to be applied to receive a more accurate measurement of the applied voltage pulse.

4.2 Discharge development in different liquids

The discharge development of the plasma inside different liquids is captured by shadowgraph imaging. The discharge is divided into four stages.

The first stage takes place during the first 28 ns after the first ignition. Table A.1 in the appendix shows the temporal evolution of the ignition in different liquids. The images of the ignition in distilled water and ethanol are taken at the same settings at a voltage of 20 kV and 1 Hz to highlight the differences between the plasma discharges. As the breakdown voltage in sodium chloride is approximately 24 kV for an electrode configuration with a 50 µm tungsten wire, the settings have to be changed to capture the ignition. While the images in distilled water and ethanol are taken with background light of the Xenon lamp, no background lighting was used for capturing the ignition in sodium chloride. This change was necessary to improve the contrast of the light emission of the plasma and background illumination. While the ignition in distilled water is very strong and can be seen by eye, the intensity of the ignition in ethanol is remarkably weaker. In sodium chloride, the ignition cannot be seen by eye but can only be captured with 100 accumulations. These accumulations are needed to separate the ignition from the background noise.

The breakdown voltage strongly depends on the medium and the electrode configuration. The breakdown voltage is higher using the 387 µm than the 50 µm tungsten wire. This matches the findings of Kolb et al. [22] and Adler [21] as the electric field inversely depends on the effectively stressed electrode area (eq. 2.6). Therefore, the needed field strength for breakdown is exceeded at different voltages for wires of different radii.

In distilled water, the plasma ignites twice. A first ignition takes place from 449 ns to 455 ns after the trigger signal. In the following, the time of the first ignition will be set to 0 ns and the time axis will be shifted accordingly. In the following 4 ns, no ignition can be observed. This time period is identified as the dark phase. As the temporal change of the applied voltage is zero, the discharge extinguishes. From 12 ns to 22 ns, the plasma ignites again. Its intensity is strongest around 16 ns. The second ignition extinguishes at 24 ns and a shaded area around the tip of the wire appears. Due to the strong emission of the plasma, this area might have been present during the discharge. As the area is noticeably developed as the plasma extinguishes and a shade around the tip during the dark phase can be seen, its presence at an earlier point in time is likely. Therefore, the shaded area can be identified as a dense distribution of streamers. This implies the mechanism of streamer-leader breakdown in water for this electrode configuration and voltage.

The ignition inside ethanol for a voltage of 20 kV is less intense than in water. A first weak light emission can be observed at 0 ns. At later stages, a second ignition cannot be observed. This implies that either sufficient electric field strengths for a second breakdown cannot be reached at a voltage of 20 kV in ethanol or that, indeed, there is a second emission which too weak to be captured by the camera. As there is a small shaded area around the tip of the wire at 26 ns, a streamer-leader mechanism is believed to be the breakdown mechanism in ethanol.

In sodium chloride, the ignition is the weakest. The ignition takes place from

0 ns to 12 ns. Therefore, it seems to be longer than the ignition in the other fluids. The appearance of a single ignition is caused by the gate of 20 ms which is needed to capture enough light. At lower gate times, the intensity of the plasma was too weak to be seen on camera. As the conductivity of sodium chloride is about 1.4 $mS\,cm^{-1}$, it is three orders of magnitude larger than the conductivity of distilled water and ethanol. Therefore, the electric field strength is weaker and the breakdown voltage higher. This increase of the breakdown voltage could be observed. Furthermore, the electric current can travel more easily through the liquid which explains the low light emission of the plasma.
In sodium chloride, no distinct region of contrast change could be determined after ignition with background illumination. Therefore, the breakdown mechanism cannot be assessed.

In literature, the dependence of the breakdown on the conductivity has not been clarified yet [11]. The breakdown in liquids has to be independently regarded for different polarities. While the electric breakdown has been found to be independent of the conductivity in non-polar fluids, Lesaint [38] observed an influence of the conductivity on breakdown phenomena in water. Therefore, breakdown in polar liquids is expected to be dependent on the conductivity. Additionally, the electrode configuration and the characteristics of the applied voltage pulse affect the dependence of electrical breakdown on the conductivity [11, 39]. Consequently, variations in the dependence can be observed for different experimental setups.

The ignition characteristics observed match the literature. After the first ignition, a phase without ignition appeared with the length of the plateau of the voltage pulse. This phase was identified as the dark phase reported in [27]. The dark phase was followed by a second ignition. This behaviour has also been observed in [26] and [28].

The streamer-leader mechanism has been found to be predominant in dielectrics and fluids with low conductivity [38]. This matches the optical analysis of the breakdown in distilled water and ethanol. The breakdown mechanism in highly conductive fluids is highly dependent on the experimental properties [24].

The second stage covers the time phase when gas channels and the shockwave evolve. The images of the second phase are shown in table A.2 in the appendix. While the streamers in distilled water are distinct, channel development in ethanol is very weak and cannot be identified in sodium chloride. Therefore, a darkened area develops around the tungsten wire. This emphasises the formation of a gaseous area around the wire. The formation of a vapour layer around the electrode for plasma discharges in 0.9 % sodium chloride has also been reported of in [40, 41, 42]. Additionally, the shape of the shockwave differs for the different liquids. While the shockwave in distilled water and ethanol feature a circular shockwave around the tip of the wire, in sodium chloride a shockwave evolves around the whole wire and therefore has an elongated shape. The shape of the shockwave seems to depend on the electrode configuration as for the 387 µm used in schlieren imaging, a circular shockwave was observed inside all the media (tab. A.5). As different electrode configurations produce different electric fields, this is believed to be a key factor for the behaviour of the shockwave.

The third phase last from 951 ns to 10 µs (tab. A.3). During this period, the gas channels merge into a gas bubble which grows in size. The images were taken in 500 ns steps. The size of the bubble does not only depend on the liquid, as the bubble growth is stronger in distilled water than in ethanol and sodium chloride, but also on the applied voltage. The diameter of the bubble increases with rising voltage amplitudes. Significant oscillations have not been observed during the bubble's growth.

Finally, the gas bubble collapses and separates from the tip (tab. A.4). First, it accelerates towards the anode but loses its momentum. Afterwards, it slowly rises towards the surface due to buoyancy forces. The velocity of the rise depends on the size of the bubble which grows with increasing voltage. The rising velocity of the bubbles inside distilled water has been estimated to a 4 mm s^{-1} to 9 mm s^{-1} for voltages between 16 kV to 24 kV. The calculation of the velocity was executed by analysing the bubbles' motion from video recordings.

As this thesis focuses on the development of the shockwave formation during the second phase, this time period has been investigated in detail to estimate shockwave propagation velocities and pressure which are presented in the following. For a more detailed description of the breakdown process inside liquids, streamer evolution is of interest as well as a quantitative analysis of the bubble growth and channel propagation as further possibilities for pressure calculation at different time stages.

4.3 Shockwave analysis

The shockwave caused by the discharge is analysed by estimating the velocities from both shadowgraphy and schlieren imaging.

Shadowgraphy

The shadowgraphy images are taken for voltages from 12 kV to 30 kV in steps of 2 kV to estimate the breakdown voltage inside the liquids. The frequency is set to 1 Hz to eliminate the possibility of an overlap of the shockwaves. The radius of the shockwave is estimated from the distance between a pixel on the outer edge of the shockwave and the centre pixel of the shockwave at an early stage of its development. The pixel width of the shockwave is calibrated with the calibration factor given in section 3.4.1.

The images are taken in steps of 50 ns. For each time step, the radius is determined for 10 different images. The weighted mean value is plotted against the time. The slope of the graph corresponds to the velocity of the shockwave. As the velocity is expected to be constant after a few nanoseconds after the ignition, a linear fit is chosen [25, 33]. The error of the slope is calculated from the method of York et al. [43].

The radius of the shockwave in distilled water at a voltage of 20 kV and frequency of 1 Hz is shown in figure 4.3.1. The time axis is shifted by 449 ns to the point of ignition. The development of the radius appears to increase linearly. All graphs

for the temporal evolution of the radii inside distilled water, ethanol and sodium chloride are shown in section A.1.2 in the appendix. The velocities which correspond to the slope of the graphs are shown in figure 4.3.2.

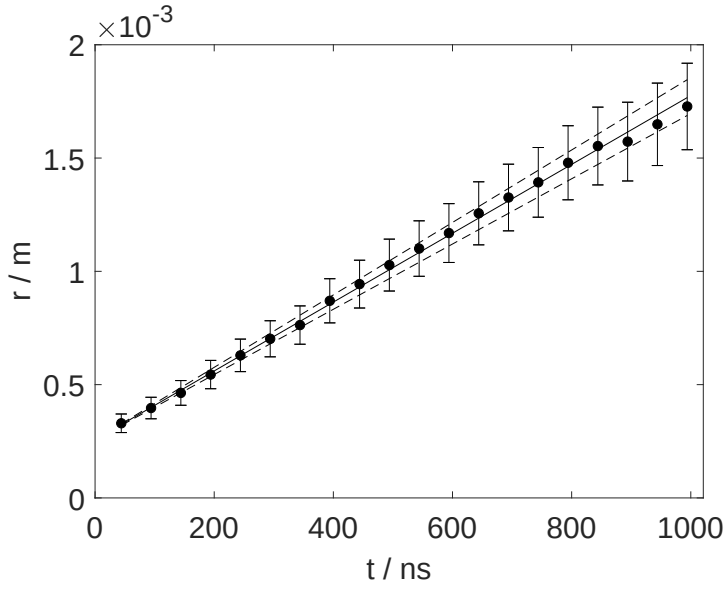

Figure 4.3.1: Radius of shockwave in distilled water at 20 kV and 1 Hz. It is displayed by the solid line. The confidence range is illustrated by the dashed lines.

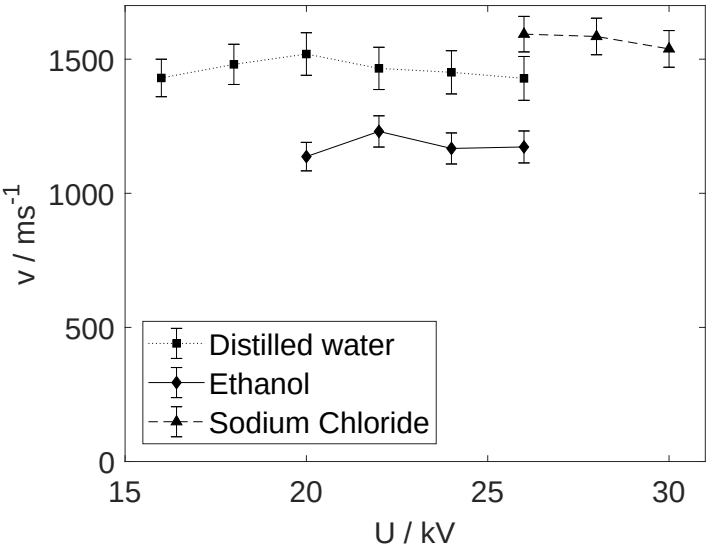

Figure 4.3.2: Shockwave velocities in distilled water, ethanol and sodium chloride.

The shockwave velocities stay approximately constant for different voltages (fig. 4.3.2). The shockwave velocities were estimated to an average of $1463 \pm 78\,\mathrm{m\,s^{-1}}$ in distilled water, $1177 \pm 57\,\mathrm{m\,s^{-1}}$ in ethanol and $1572 \pm 68\,\mathrm{m\,s^{-1}}$ in 0.9 % sodium chloride.

These velocities match the speed of sound in different media. The speed of sound in water at a water temperature of 23 °C is $1491.50 \pm 2.87\,\mathrm{m\,s^{-1}}$ [44], $1160.2\,\mathrm{m\,s^{-1}}$ in ethanol at a fluid temperature of 20 °C [45] and $1498\,\mathrm{m\,s^{-1}}$ at 22 °C in 0.9 % sodium chloride [46, 47].

The velocities investigated by shadowgraphy do not cover the early stages of the development of the shockwave. While the shockwave proceeds with the speed of sound after a few nanoseconds, the velocities must be higher during the first nanoseconds after ignition. This can be observed in figure 4.3.1. The linear fit does not pass the origin if extrapolated to earlier stages but would reach a radius of zero prior to t = 0 ns and therefore before the ignition takes place. Instead, the velocity must be much higher during the first 44 ns.

This phenomenon is studied in different liquids at different voltages. The initial radii of the shockwave at 44 ns after ignition are plotted in figure 4.3.3a. For all media, the shockwaves' radius is significantly higher than 100 µm at 44 ns after ignition. The shockwaves' initial velocity must be larger than $2272.2\,\mathrm{m\,s^{-1}}$ if the shockwave is expected to evolve with the first discharge. This velocity is much larger than the speed of sound in all media. Furthermore, the radius of the shockwave 44 ns after the first discharge increases with increasing voltage. Consequently, the initial velocity must also increase with an increasing voltage. This trend is shown in figure 4.3.3b.

An estimation based on the radii $r_{44\,ns}$ of the shockwave 44 ns after ignition (fig. 4.3.3a) was made to estimate the initial velocities. The time of ignition t was expected to be constant with an uncertainty of 2 ns.

The velocities v_i and their errors Δv_i were calculated as

$$v_i = \frac{r_{44\,ns}}{t} \tag{4.1}$$

$$\Delta v_i = \sqrt{\left(\frac{1}{t} \cdot \Delta r_{44\,ns}\right)^2 + \left(-\frac{r_{44\,ns}}{t^2} \cdot \Delta t\right)^2}\,. \tag{4.2}$$

The initial shockwave velocities are plotted in figure 4.3.3b. All velocities are in a supersonic range. In distilled water, the initial velocities increase from $5600\,\mathrm{m\,s^{-1}}$ to $8900\,\mathrm{m\,s^{-1}}$. In ethanol, the velocities are significantly lower. For a voltage of 20 kV, the initial velocity is $3400\,\mathrm{m\,s^{-1}}$ and increases to $4800\,\mathrm{m\,s^{-1}}$. In sodium chloride, the initial velocity increases from $4080\,\mathrm{m\,s^{-1}}$ to $4800\,\mathrm{m\,s^{-1}}$.

Consequently, there must be a dependence of the initial shockwave velocity on the applied voltage pulse, while the shockwave velocity at later stages is independent of the voltage. Thus, the shockwave expansion must be separated into two different stages.

The first stage is set during the first 50 ns after the first plasma discharge. During this time period, the shockwave expands at supersonic speed. During the first nanoseconds after the voltage pulse is applied, the streamer formation and discharge take place. Supersonic streamer and shockwave expansion inside liquids has been observed by several groups [20, 26, 48, 49]. An, Baumung, and

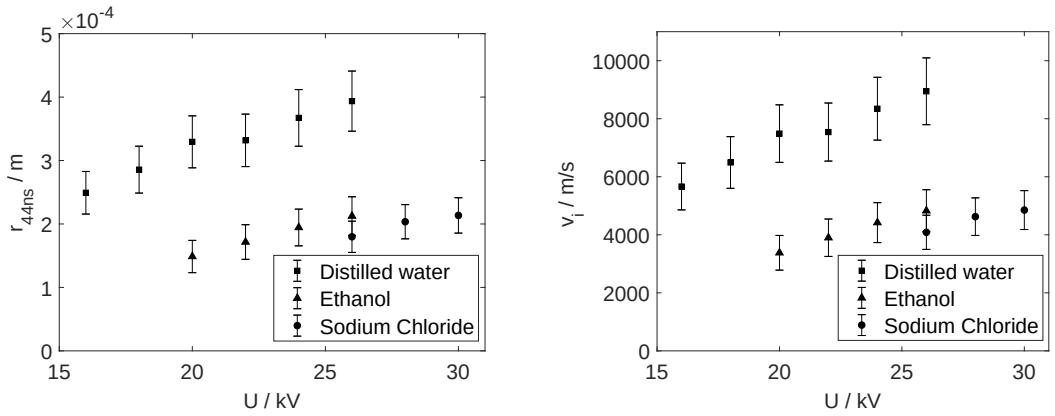

(a) Radii of the shockwave 44 ns after the plasma ignition.

(b) Minimum initial shockwave velocity derived from radii in figure 4.3.3a.

Figure 4.3.3: Initial radii of the shockwave and the initial velocities derived from these radii taken at 44 ns after plasma ignition.

Bluhm have studied streamer development for a pin-to-plate geometry. At a voltage of 18 kV with an unknown pulse length, a streamer propagation velocity of 2500 m s^{-1} was found. As the discharge and streamer propagation are supersonic mechanisms, it is expected that a shockwave caused by these phenomena develops at supersonic speed.

As the formation of the shockwave is believed to be closely related to the streamer development [20], initial supersonic shockwave velocities match this proposition.

The phenomenon of an increased initial velocity of a shockwave in water that reduces to the speed of sound after approximately 50 ns has also been reported by Marinov et al. [33] and Pushkin et al. [50]. Marinov et al. [33] have found initial velocities of 2200 m s^{-1} for an applied voltage of 4 kV and 4200 m s^{-1} for a voltage of 9 kV. The order of magnitude of the initial shockwave propagation velocity and the increase of the shockwave velocity with increasing voltage matches the findings in this thesis.

The second stage begins approximately 50 ns after the first discharge (fig. 4.3.1). The shockwave velocity reduces to the speed of sound and propagates constantly at this speed. No second relaxation of the shockwave was observed. Similar time scales were observed by Marinov et al. [33] as they found a decrease of the initial velocity after 50 ns to 70 ns.

The differences between the initial velocities may correspond to the different electric conductivities of the liquids. As the sodium chloride solution is highly conductive, the current travels easily through the liquid and the electric field that forms around the electrode is not as strong as in liquids with a low conductivity. As the streamer length has been found to be dependent on the conductivity of the liquid [51], the initial pressure in the vicinity of the electrode may be influenced by the conductivity as the streamer and channel development depends on the conductivity. In contrary, Vankov and Palanker [42] report of a streamer velocity of 3 km s^{-1} in distilled water and a saline solution. Further investigation of the streamer development in distilled water, ethanol and sodium chloride needs

to be performed to estimate the dependence of the streamer development and shockwave velocity on the conductivity of a liquid.

In conclusion, the shockwave propagation consists of two phases. The first phase is characterised by fast streamer development causing compression waves at supersonic speed. After 50 ns, the second stage sets in and the shockwave velocity reduces to a constant velocity of the speed of sound.

To improve the accuracy of the velocity determined from shadowgraph images, the following improvement should be made.
The calibration of the image is of crucial importance to improve the velocity measurements. Due to the narrow width of the wire, the calibration factor has a large error. Instead of a narrow wire, a wire which covers a large section of the shadowgraph image should be chosen for the calibration. This improvement has been made for the schlieren imaging as described in 3.4.2. Further errors are caused by the weak contrast of the shockwave, especially in sodium chloride. A background subtraction was not possible due to movement of the wire. A more rigid wire should also be used for shadowgraph imaging to suppress this movement. This would allow background subtraction to improve the estimation of the position of the shockwave. Furthermore, errors caused by scratches on the lenses and an inhomogeneous illumination of the lamp cause a minor image quality. The illumination of the Xenon lamp can be adjusted by an internal lens but at a homogeneous illumination, the intensity is too weak and the contrast between shockwave and background is not visible. An alternative to the Xenon lamp is the use of a laser. This light source offers a higher intensity and the beam path can be controlled more easily. Furthermore, a small light source reduces the amount of blur of a shadowgraph image [37].

For an analysis of smaller non-uniformities such as streamer formation and channel propagation, the quality of the shadowgraph image needs to be improved. A setup similar to the schlieren setup (fig. 3.4.2) with removal of the razor blade is more suitable as it offers a sharper image. The path of the light beam can be easily adjusted with plane mirrors and the diameter of the light beam can be adjusted by changing the length of the light path and the diameter of the aperture.

Schlieren imaging

The schlieren images are taken to verify the velocities estimated from the shadowgraph images. As the schlieren images are weak in contrast due to the low light intensity, each image is taken with 20 accumulations. As the breakdown voltage is higher for this configuration, all images are taken at 30 kV at a frequency of 1 Hz. The velocity is calculated by the same method as the shadowgraph images. For the uncertainty of the pixel position of the shockwave, a value of 20 pixel is set as the read-out inaccuracy.

The schlieren images at four different time stages are given in table A.5 in the appendix. The time is shifted by 478 ns to the point of the first ignition. The tungsten wire is on the left-hand side of the image. Lighter regions are caused by areas of reduced density inside the liquid.

In distilled water, a blurred, circular lighter region is visible around the tip. This

region is already significantly separated from the tip. In the following images, the circular region moves towards the outside. At 245 ns, the region inside the light circle is still slightly lighter than the outside. In the following, the circular region grows without visible differences inside.

The lighter area shows the streamers at an early stage and later the shockwave inside the liquids. The frayed edge of the shockwave at 45 ns could be caused by streamer development which may also cause the lighter region inside the shockwave at 245 ns.

In ethanol, a light region exists close to the tip at 45 ns. It grows to a circular region. The size of the region of reduced density at 45 ns is much smaller than in water. Therefore, the shockwave evolution seems to start later.

In sodium chloride, the same phenomenon can be observed. At an early point in time, the area of reduced density is only visible in the direct vicinity of the tip. In the following, a circular shockwave evolves around the tip.

Table 4.1: Shockwave velocities in distilled water, ethanol and sodium chloride at U=30 kV and f=1 Hz estimated from schlieren imaging and mean shockwave velocities estimated from shadowgraphy.

medium	$v_{schlieren}$ / $\mathrm{m\,s^{-1}}$	v_{shadow} / $\mathrm{m\,s^{-1}}$
distilled water	1382 ± 62	1463 ± 78
ethanol	1121 ± 34	1177 ± 57
0.9 % sodium chloride	1498 ± 40	1572 ± 68

The shockwave velocities are listed in table 4.1. These velocities are close to the velocities estimated from shadowgraphy and are also in the order of the speed of sound. This confirms the propagation during the second propagation stage of the shockwave at a constant velocity of the speed of sound.

A major challenge of the schlieren setup has been the occurrence of interferences. The HeNe laser does not produce a single, parallel light beam but interferences occurred. The initial interference could be avoided by the aperture in the setup but further interferences were caused due to the lenses and quartz windows of the chamber. These interferences cause circular shaped interference patterns on the image which partly cover the shockwave for long gate times. Furthermore, the razor blade had to be adjusted to a position which cuts off a large part of the laser beam to receive a schlieren image instead of a shadowgraph image. This led to a reduced intensity of the image which was too weak to analyse contrasts precisely. Thus, the images accumulate the light of 20 measurements. This causes a blur of the shock front and impairs the accuracy of the radius determined from the images.

4.4 Pressure calculation

The estimation of the pressure inside the liquid can be performed using the shockwaves' velocity as the formula for pressure calculation is velocity-dependent. For sonic waves, the pressure inside the liquid does not change significantly as no shock is formed. Therefore, the pressure inside the liquid stays approximately at atmospheric pressure.

During the first stage of the shockwave propagation, the velocity is supersonic. Therefore, a shock inside the medium can occur.

The pressure inside the liquid can be estimated from the Rankine-Hugeniot equations. Waves which propagate at supersonic speed can generate a shock inside a liquid which causes a sudden change in the pressure and density in the medium. To estimate the pressure, the velocity of the shockwave u_s and the velocity u_p of the particles after the shock and the ambient hydrostatic density ρ_0 have to be regarded [49, 52]. As the parameters for the following equations have only been estimated for water, the pressure during the first shockwave propagation phase is calculated for water only. In the following calculations, the density in water at 22 °C is 998 kg m^{-3} [53] and the atmospheric pressure is 101 325 Pa.

The velocity of the particles is presented by Rice and Walsh [54] as

$$u_p = c_1 \cdot (10^{\frac{u_s - c_0}{c_2}} - 1) \,. \tag{4.3}$$

The speed of sound inside the medium is c_0. The parameters c_1 and c_2 can be derived from the Hugeniot curve. c_1 is 5190 m s^{-1} and c_2 is 25 306 m s^{-1}.

Rice and Walsh [54] have initially studied shockwaves in a pressure range of 2.5 GPa to 25 GPa but equation 4.3 can also be applied to higher pressures as they have investigated pressures of 45 GPa for shockwaves in water.

The pressure p_s in the region compressed by the shock is given by the conservation of momentum of a shock front

$$p_s = \rho_0 u_s u_p + p_0 \tag{4.4}$$

where p_0 is the ambient hydrostatic pressure [49, 55].

The pressure can therefore be calculated by combining equations 4.3 and 4.4 to the following.

$$p_{s,RW} = c_1 \rho_0 u_s \cdot (10^{\frac{u_s - c_0}{c_2}} - 1) + p_0 \tag{4.5}$$

For pressures up to 1 GPa, Nagayama et al. [52] present a method to estimate the pressure caused by a shock inside water from the velocity of the shock front (4.6).

$$p_{s,N} = \rho_0 u_s \frac{u_s - A}{B} \tag{4.6}$$

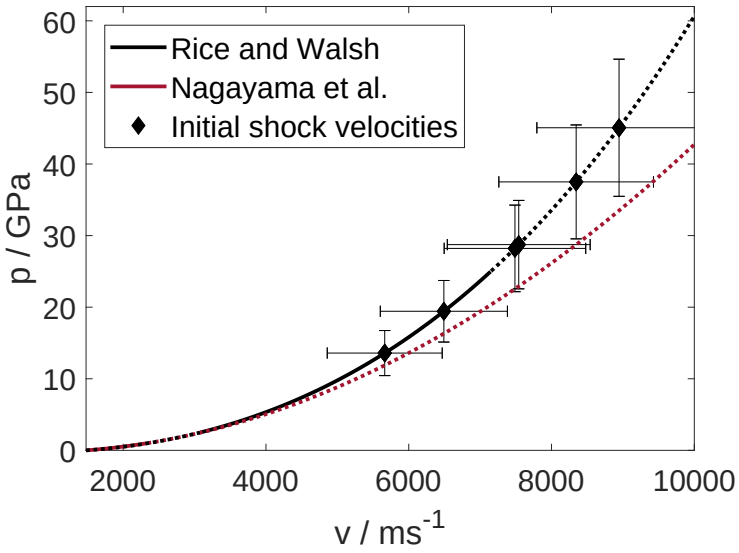

Figure 4.4.1: Pressure curves of shockwaves in water according to equations 4.5 (black) and 4.6 (red). Solid line marks the definition range of the method, the dotted curves are values outside the methods pressures range. Experimental velocity data are marked as symbols on plot.

The parameters $A = 1450\,\mathrm{m\,s^{-1}}$ and $B = 1.99$ have been calculated from the relationship between shock velocity and particle velocity [52].

The methods for pressure calculations of underwater shockwaves are commonly used in literature [48, 49, 50].

To estimate the initial pressure in the vicinity of the tip of the tungsten wire, the pressure curves are plotted in figure 4.4.1 for water according to equations 4.5 and 4.6 for shockwave velocities between the sound of speed and $10\,000\,\mathrm{m\,s^{-1}}$. The pressure values for the initial shockwave velocities (fig. 4.3.3b) are estimated for equation 4.5 as it is defined for high pressure ranges. For low velocities, both equations provide the same pressures. For high velocities, the method of Nagayama et al. underestimates the pressure. Therefore, the parameters of Rice and Walsh are used in the following.

The errors of the pressure are calculated according to equation 4.7.

$$\Delta p_{s,RW} = \parallel c_1\rho_0 \cdot \left(\left(10^{\frac{u_s - c_0}{c_2}} - 1\right) + \frac{u_s}{b} \cdot \log(10) \cdot 10^{\frac{u_s - c_0}{b}}\right) \cdot \Delta u_s \parallel \tag{4.7}$$

The initial pressures caused by the shockwave during the first 44 ns after the discharge is in a region of several GPa. As the velocity increases with increasing voltage, the pressures follow the same trend (tab. 4.2.

As the shockwave velocity during the first 44 ns could only be estimated from the radius of the shockwave after this time period, the evolution of the pressure during the first nanoseconds after the discharge cannot be analysed. As the velocity during the first shockwave propagation stage is calculated from a linear model, the initial acceleration of the shockwave is not considered in the pressure calcu-

Table 4.2: Initial pressures estimated from shockwave velocities during the first 44 ns (fig. 4.3.3b) after the discharge according to equation 4.5.

U / kV	16	18	20	22	24	26
p / GPa	14 ± 4	19 ± 5	28 ± 7	29 ± 7	38 ± 8	45 ± 10

lation. Therefore, the pressure values in table 4.2 are not valid for the entire first phase but are a reference pressure value for the average velocity during the first propagation phase. Seepersad et al. [25] propose both an exponential pressure decay in the vicinity of the electrode over time and with increasing distance from the electrode.

4.4.1 Influence of the pressure on optical emission spectra

Next to an optical analysis of the discharge, optical emission spectroscopy is a common method to gain information on the species inside a plasma, especially electron densities and gas temperatures [56]. As the information can be derived from line broadening in the spectrum, different broadening effects must be taken into consideration, when analysing the optical emission spectra. As Stark broadening and Doppler broadening are believed to be the main broadening mechanisms [57]. The influence of Van der Waals broadening, which is a pressure broadening mechanism, is estimated for the different shockwave propagation stages and will be briefly discussed. As optical emission spectroscopy has only been performed for distilled water for this setup, only Van der Waals broadening in this medium will be investigated.

Instrumental line broadening is also a characteristic broadening effect in optical emission spectroscopy but has already been subtracted from the spectra presented in this section.

Van der Waals broadening typically occurs for plasmas with low electron densities and high pressures [58].

A Lorentz profile is assumed as the profile for Van der Waals broadening. The width w_{VdW} of the spectral line caused by Van der Waals broadening is calculated according to equation 4.8.

$$w_{VdW}[nm] = 5.925 \cdot 10^{14} K_1 \cdot K_p \cdot 10^{-2} p[Pa] \cdot T[K]^{-0.7} \tag{4.8}$$

K_1 is the line coefficient and K_p is the perturber coefficient in the equation above. The temperature T is given in K and the pressure p in Pa. The pressure values are taken from figures 4.4.1. For H_α and a 3s-2p transition, K_1 is 3.402×10^{-8} [58].

As the perturber coefficients have not been estimated for water molecules in [58], the approximation presented by Marinov, Starikovskaia, and Rousseau [48] is used for further calculations (eq. 4.9). Here, the assumption is made that all perturbers are hydrogen atoms. The gas temperature is expressed by T_g.

$$w_{VdW}[nm] = 10^{-6} \cdot 6 \cdot \frac{p[Pa]}{T_g[K]^{0.7}} \tag{4.9}$$

The width of the line broadening in water depending on the gas temperature is given in figure 4.4.2 for the first shockwave propagation phase and in 4.4.3 for the second shockwave propagation phase. These values do not show accurate widths but only the magnitude of the Van der Waals broadening. As the perturber constant, temperature and pressure are only approximate values, the widths are expected to have large errors. The error of the approximation made in equation 4.9 is expected to be less than 30 % [48]. As the error of the pressures is in a region of 30 %, the inaccuracy of the Van der Waals broadening widths is expected to be approximately a factor of 2. Therefore, no confidence range is plotted in figure 4.4.2.

Still, differences between the pressure broadening effect during the first and second shockwave propagation phase can be seen clearly. During the first stage, the broadening width is in a µm range (fig. 4.4.2). For increasing gas temperatures, the Van der Waals broadening decreases but is still greater than 4 µm for voltages between 16 kV and 26 kV. Therefore, Van der Waals broadening has a strong effect on the line width in emission spectra during the first 50 ns. Depending on the pressure decay, this time span may vary in length.

During the second stage, the pressure reduces to approximately ambient pressure. The Van der Waals broadening width decreases under 1 nm for temperatures between 300 K and 10 000 K.

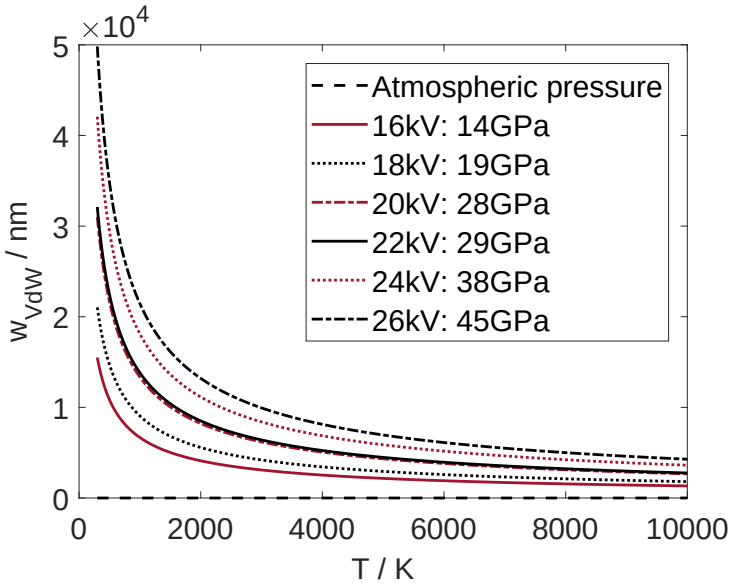

Figure 4.4.2: Van der Waals broadening depending on the gas temperatures between 300 K and 10 000 K for pressures at voltages between 16 kV and 26 kV during the first shockwave propagation phase.

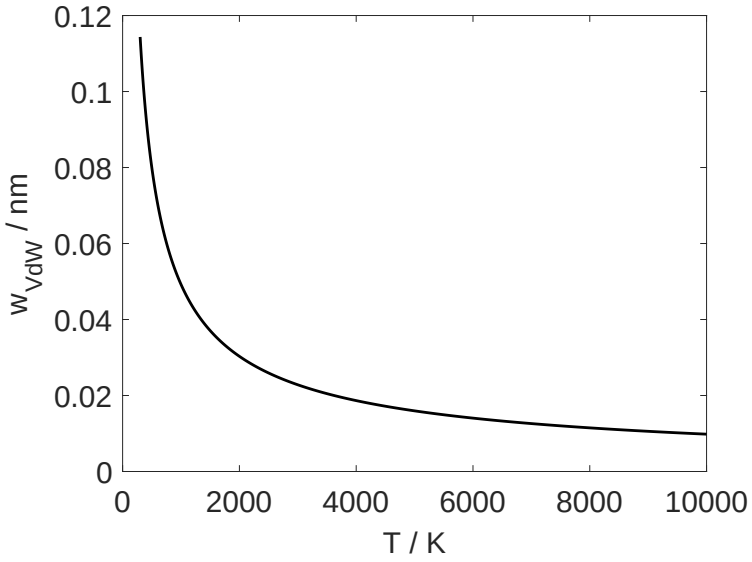

Figure 4.4.3: Van der Waals broadening depending on the gas temperatures between 300 K and 10 000 K for atmospheric pressure during the second shockwave propagation phase.

Data for time resolved optical emission spectroscopy performed previously at 20 kV and 15 Hz with a gate of 30 ns is presented in figures 4.4.4 and 4.4.5. The time is set to zero just before the plasma ignites. The first 60 ns are presented in figure 4.4.4. As a reference, the intensity was measured before the ignition and is close to zero. After the ignition, a continuum forms and no spectral lines can be detected until 60 ns after the ignition. This matches with the findings above, as Van der Waals broadening is strongly pronounced during the first 50 ns after the discharge and decreases to less than 1 nm. This corresponds with the data presented in figure 4.4.5, as the H_{alpha} line at 656 nm can be clearly distinguished.

A strong broadening of the H_α line has also been reported of in [48, 57]. Marinov, Starikovskaia, and Rousseau [48] propose that the decay of the width of the H_α line is caused by a relaxation of the pressure inside the gas channels. This matches the results presented in this thesis as the timescale of an increased pressure in the vicinity of the electrode and the strong broadening of the H_α line are similar. Additionally, recombination and collisions of particles after the discharge are effects that need to be taken into consideration when analysing the spectra which are taken directly after the discharge. Assuming an exponential pressure decay, Van der Waals broadening should only occur directly after the discharge and does not influence the width of the lines in optical emission spectra taken at later times.

To estimate the pressure in the vicinity of the electrode during the second shockwave propagation phase, streamer and channel development need to be investigated. As the shockwave travels away from the electrode, the pressure of the shock front is not always at the same position but the pressure peak moves away [25]. As the channels develop in the direct vicinity of the electrode tip, an estimation of the pressure from the channel expansion as demonstrated in [20] and [48] provides more accurate pressure values to estimate the impact of pressure

broadening, in particular Van der Waals broadening, on optical emission spectra for a further analysis of the plasma discharge.

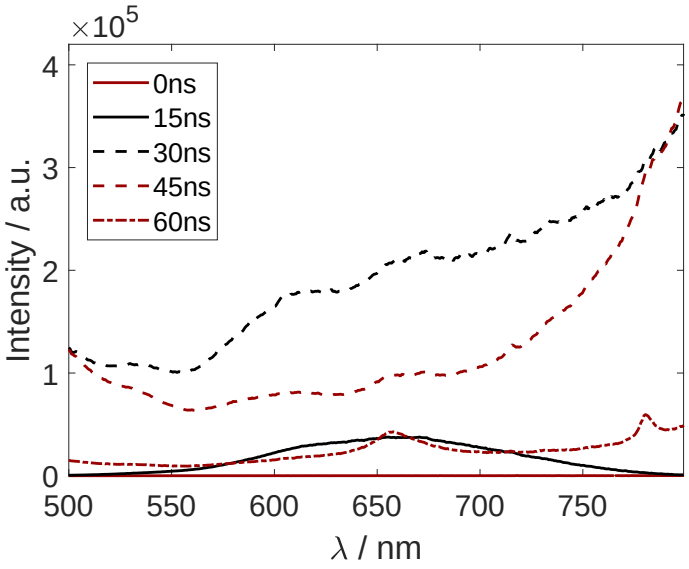

Figure 4.4.4: Optical emission spectrum of a plasma discharge in distilled water at 20 kV and 15 Hz during the first 60 ns after the first ignition [K. Grosse, personal communication, September 12, 2018].

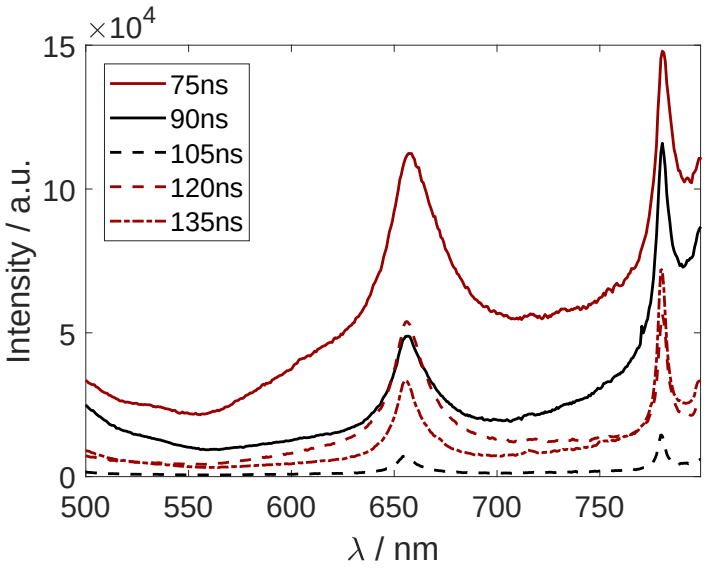

Figure 4.4.5: Optical emission spectrum of a plasma discharge in distilled water at 20 kV and 15 Hz between 75 ns and 135 ns after the first ignition [K. Grosse, personal communication, September 12, 2018].

A camera with multiple CCD chips is needed to visualise the development of a single streamer or gas channel. The Andor iStar camera used in this setup for

shadowgraphy and schlieren imaging can only take one image per voltage pulse. Therefore, the setup needs to be adapted accordingly to investigate the development of a single discharge.

In conclusion, pressure broadening estimated from the shockwave propagation has been found to be significant directly after the discharge but as the pressure reduces to atmospheric pressure, the influence of Van der Waals broadening on the line width in optical emission spectra can be neglected.

5. Conclusion and Outlook

During the optical analysis of a nanosecond plasma ignited inside distilled water, ethanol and 0.9 % sodium chloride at different voltages, the discharge behaviour and streamer evolution, the formation and propagation of a shock wave and formation of a bubble were investigated. Furthermore, the shape of the voltage pulse and its behaviour were analysed and current measurements were attempted.

Measurements of a nanosecond voltage pulse with short rise times behave differently depending on the voltage cable. Due to the fast rise time, a large amount of electromagnetic interference is produced whose amplitude depends on the selection of the cables used. This interference cannot be reduced completely with shielding and disturbs the voltage and current signal significantly. The use of a high voltage cable made from one piece with a minimum amount of solder joints is recommended to minimise the amount of interference and allow precise voltage measurements for a detailed analysis of the amplitude and shape of the voltage pulse.

In distilled water, the ignition can be divided into a first ignition, dark phase and second ignition which are consistent with the shape of the voltage pulse. If there is no temporal change of the voltage, the plasma deceases. This happens during the plateau of the voltage pulse whose length matches the duration of the dark phase. In ethanol and sodium chloride the ignition is too weak under the studied conditions to be compared to the shape of the voltage pulse.

Streamer formation in the vicinity of the electrode tip can be observed inside distilled water and ethanol. Therefore, streamer-leader breakdown is considered as the most likely breakdown phenomenon. Channel formation is very noticeable in distilled water and weak in ethanol. In sodium chloride, no streamers could be observed. Instead, the wire appears to be surrounded by a narrow gas layer.

The propagation of a shockwave is assigned to two phases. The pressures inside the liquid are estimated for liquid water. In distilled water, the pressure varies from (14 ± 4) GPa to (45 ± 10) GPa depending on the applied voltage. The shockwave travels at supersonic speed in distilled water, ethanol and sodium chloride and its initial velocity increases with increasing voltage amplitudes. During the second phase, the shockwave's acceleration stops and its velocity reduces to the speed of sound in the local medium. The pressures reduce to atmospheric pressure, as no shock inside the medium is generated during the second phase.

For further investigation of species created inside this the liquid in this setup, optical emission spectroscopy needs to be performed. The knowledge of the magnitude of the pressure is needed to estimate the impact of pressure broadening on the lines in optical emission spectroscopy as electron densities can be derived from these spectra. Pressure broadening has been found to be significant directly after the plasma discharge as the Van der Waals broadening can be as high as several µm depending on the gas temperature. As the pressure relaxes, Van der Waals broadening decreases to under 1 nm and is therefore negligible. A compar-

ison of the Van der Waals broadening with emission spectra in water for the same setup has shown good correspondence as no distinct line is visible until 60 ns after the discharge. Instead, the spectrum seems continuous during this time span which is expected to be impacted by the pressure broadening.

On a µs scale, a bubble forms which constantly grows in size to a specific radius before it collapses. The bubble separates from the electrode tip after the collapse.

This knowledge of the discharge behaviour of the nanosecond plasma for a pin-to-pin setup is essential for a better understanding of the impact of the voltage supply on the discharge behaviour and further analysis of the plasma's characteristics.

As the pressure could only be estimated from the shockwave propagation during the first 44 ns and the peak pressure caused by the shockwave in the liquid propagates with the shockwave away from the electrode, the pressure may differ in the vicinity of the electrode from the finding presented for later time stages. An analysis of the streamer and channel expansion using a camera with multiple CCD chips needs to be performed to estimate the impact of pressure broadening on optical emission spectra not only directly after the ignition but also at later times.

Bibliography

[1] B. R. Locke et al.: Electrohydraulic Discharge and Nonthermal Plasma for Water Treatment. *Industrial & Engineering Chemistry Research* 45.3, 2006.

[2] M. Sato, T. Ohgiyama, and J. S. Clements: Formation of chemical species and their effects on microorganisms using a pulsed high-voltage discharge in water. *IEEE Transactions on Industry Applications* 32.1, 1996.

[3] W. G. Graham and K. R. Stalder: Plasmas in liquids and some of their applications in nanoscience. *Journal of Physics D: Applied Physics* 44.17, 2011.

[4] J. Gubkin: Electrolytische Metallabscheidung an der freien Oberfläche einer Salzlösung. *Annalen der Physik* 268.9, 1887.

[5] J. Foster et al.: Perspectives on the Interaction of Plasmas With Liquid Water for Water Purification. *IEEE Transactions on Plasma Science* 40.5, 2012.

[6] R. J. Gilliom et al.: *Pesticides in the Nation's Streams and Ground Water, 1992-2001*. 2006.

[7] P. C. Vandevivere, R. Bianchi, and W. Verstraete: Review: Treatment and reuse of wastewater from the textile wet-processing industry: Review of emerging technologies. *Journal of Chemical Technology & Biotechnology* 72.4, 1998.

[8] M. S. Reisch: Asian Textile Dye Makers Are A Growing Power In Changing Market. *Chemical & Engineering News* 74, 1996.

[9] United States Environmental Protection Agency: *History of Drinking Water Treatment*. Tech. rep. 2000.

[10] S. Parsons: *Advanced Oxidation Processes for Water and Wastewater Treatment*. IWA Publishing, 2004.

[11] P. Bruggeman and C. Leys: Non-thermal plasmas in and in contact with liquids. *Journal of Physics D: Applied Physics* 42.5, 2009.

[12] A. Hamdan et al.: Interaction of Discharges in Heptane with Silicon Covered by a Carpet of Carbon Nanotubes. *Advanced Engineering Materials* 15.10, 2013.

[13] K. R. Stalder et al.: Repetitive plasma discharges in saline solutions. *Applied Physics Letters* 79.27, 2001.

[14] T. Kaneko, K. Baba, and R. Hatakeyama: Gas–liquid interfacial plasmas: basic properties and applications to nanomaterial synthesis. *Plasma Physics and Controlled Fusion* 51.12, 2009.

[15] P. J. Bruggeman et al.: Plasma–liquid interactions: a review and roadmap. *Plasma Sources Science and Technology* 25.5, 2016.

[16] F. F. Chen: *Introduction to Plasma Physics and Controlled fusion*. 2nd edition. Plenum Press, 1984.

[17] A. Fridman: *Plasma Chemistry*. Cambridge University Press, 2008.

[18] J. M. Meek and J.D. Craggs: *Electrical Breakdown Of Gases*. Oxford At The Clarendon Press, 1953.

[19] A. I. Gerasimov: Water as an insulator in pulsed facilities (Review). *Instruments and Experimental Techniques* 48.2, 2005.

[20] W. An, K. Baumung, and H. Bluhm: Underwater streamer propagation analyzed from detailed measurements of pressure release. *Journal of Applied Physics* 101.5, 2007.

[21] R. J. Adler: *2013 Version - Pulsed Power Formulary*. North Star Research Corporation, 2013.

[22] J. F. Kolb et al.: Streamers in water and other dielectric liquids. *Journal of Physics D: Applied Physics* 41.23, 2008.

[23] K. Schoenbach et al.: Electrical breakdown of water in microgaps. *Plasma Sources Science and Technology* 17.2, 2008.

[24] D. V. Tereshonok et al.: Pre-breakdown phenomena and discharges in a gas-liquid system. *Plasma Sources Science and Technology* 27.4, 2018.

[25] Y. Seepersad et al.: On the electrostrictive mechanism of nanosecond-pulsed breakdown in liquid phase. *Journal of Physics D: Applied Physics* 46.16, 2013.

[26] A. Starikovskiy et al.: Non-equilibrium plasma in liquid water: dynamics of generation and quenching. *Plasma Sources Science and Technology* 20.2, 2011.

[27] D. Dobrynin et al.: Non-equilibrium nanosecond-pulsed plasma generation in the liquid phase (water, PDMS) without bubbles: fast imaging, spectroscopy and leader-type model. *Journal of Physics D: Applied Physics* 46.10, 2013.

[28] Y. Seepersad et al.: Investigation of positive and negative modes of nanosecond pulsed discharge in water and electrostriction model of initiation. *Journal of Physics D: Applied Physics* 46.35, 2013.

[29] M. N. Shneider and M. Pekker: Dielectric fluid in inhomogeneous pulsed electric field. *Phys. Rev. E* 87, 4 2013.

[30] N. J. Felici: Blazing a fiery trail with the hounds (prebreakdown streamers). *IEEE Transactions on Electrical Insulation* 23.4, 1988.

[31] T. J. Lewis: A new model for the primary process of electrical breakdown in liquids. *IEEE Transactions on Dielectrics and Electrical Insulation* 5.3, 1998.

[32] I. Marinov et al.: Modes of underwater discharge propagation in a series of nanosecond successive pulses. *Journal of Physics D: Applied Physics* 46.46, 2013.

[33] I. Marinov et al.: Cavitation in the vicinity of the high-voltage electrode as a key step of nanosecond breakdown in liquids. *Plasma Sources Science and Technology* 22.4, 2013.

[34] S. Ridah: Shock waves in water. *Journal of Applied Physics* 64.1, 1988.

[35] V. Y. Ushakov, V. F. Klimkin, and S. M. Korobeynikov: *Impulse Breakdown of Liquids*. Power Systems. Springer Berlin Heidelberg, 2007.

[36] G. de Izarra and C. de Izarra: Quantitative shadowgraphy made easy. *European Journal of Physics* 33.6, 2012.

[37] E. Traldi et al.: Schlieren imaging: a powerful tool for atmospheric plasma diagnostic. *EPJ Techniques and Instrumentation* 5.1, 2018.

[38] O. Lesaint: Prebreakdown phenomena in liquids: propagation 'modes' and basic physical properties. *Journal of Physics D: Applied Physics* 49.14, 2016.

[39] V. Y. Ushakov, O. P. Semkina, and V. V. Ryumin: On the nature of pulse electric breakdown of aqueous electrolytes. *Appl. Electr. Phenom.* 2, 1972.

[40] L. Schaper, W. G. Graham, and K. R. Stalder: Vapour layer formation by electrical discharges through electrically conducting liquids—modelling and experiment. *Plasma Sources Science and Technology* 20.3, 2011.

[41] L. Schaper, K. R. Stalder, and W. G. Graham: Plasma production in electrically conducting liquids. *Plasma Sources Science and Technology* 20.3, 2011.

[42] A. Vankov and D. Palanker: Nanosecond plasma-mediated electrosurgery with elongated electrodes. *Journal of Applied Physics* 101.12, 2007.

[43] D. York et al.: Unified equations for the slope, intercept, and standard errors of the best straight line. *American Journal of Physics* 72.3, 2004.

[44] M. Greenspan and C.E. Tschiegg: Speed of sound in water by a direct method. *J. Res. Natl. Bur. Stand.* 59.4, 1957.

[45] R. Wegge, M. Richter, and R. Span: Speed of Sound Measurements in Ethanol and Benzene over the Temperature Range from (253.2 to 353.2) K at Pressures up to 30 MPa. *J. Chem. Eng. Data* 60.5, 2015.

[46] *Technical Guides - Speed of Sound in Sea-Water*. National Physical Laboratory. URL: `http://resource.npl.co.uk/acoustics/techguides/soundseawater/content.html#UNESCO`, visited on 09/16/2018.

[47] A. B. Coppens: Simple equations for the speed of sound in Neptunian waters. *The Journal of the Acoustical Society of America* 69.3, 1981.

[48] I. Marinov, S. Starikovskaia, and A. Rousseau: Dynamics of plasma evolution in a nanosecond underwater discharge. *Journal of Physics D: Applied Physics* 47.22, 2014.

[49] A. Vogel, S. Busch, and U. Parlitz: Shock wave emission and cavitation bubble generation by picosecond and nanosecond optical breakdown in water. *The Journal of the Acoustical Society of America* 100.1, 1996.

[50] A. Pushkin et al.: Cavitation and shock waves emission on the rigid boundary of water under mid-IR nanosecond laser pulse excitation. 15, 2018.

[51] J. S. Clements, M. Sato, and R. H. Davis: Preliminary Investigation of Prebreakdown Phenomena and Chemical Reactions Using a Pulsed High-Voltage Discharge in Water. *IEEE Transactions on Industry Applications* IA-23, 1987.

[52] K. Nagayama et al.: Shock Hugoniot compression curve for water up to 1 GPa by using a compressed gas gun. *Journal of Applied Physics* 91.1, 2002.

[53] M. O. McLinden E. W. Lemmon and D. G. Friend: Thermophysical Properties of Fluid Systems. *NIST Standard Reference Database 69: NIST Chemistry WebBook*, ed. by P.J. Linstrom and W.G. Mallard. Visited on 09/16/2018.

[54] M. H. Rice and J. M. Walsh: Equation of State of Water to 250 Kilobars. *The Journal of Chemical Physics* 26.4, 1957.

[55] W. Band: *Introduction to Mathematical Physics*. Princeton, NJ: Van Nostrand, 1959.

[56] P. Bruggeman et al.: Optical emission spectroscopy as a diagnostic for plasmas in liquids: opportunities and pitfalls. *Journal of Physics D: Applied Physics* 43.12, 2010.

[57] B. Pongrac et al.: Spectroscopic characteristics of H_α / O^I atomic lines generated by nanosecond pulsed corona-like discharge in deionized water. *Journal of Physics D: Applied Physics* 51.12, 2018.

[58] N. Konjević, M. Ivković, and N. Sakan: Hydrogen Balmer lines for low electron number density plasma diagnostics. *Spectrochimica Acta Part B: Atomic Spectroscopy* 76, 2012.

6. Danksagung

Abschließend möchte ich die Möglichkeit nutzen, meine Dankbarkeit an alle Menschen auszudrücken, welche mich auf dem Weg der Erarbeitung und Erstellung dieser Arbeit unterstützt haben. Ein besonderer Dank geht hierbei an

- Prof. Dr. Achim von Keudell, der mir die Möglichkeit gegeben hat, am Lehrstuhl für Experimentalphysik II zu arbeiten und diese Arbeit zu erstellen.
- Dr. Mark Böke, der sich zur Zweitkorrektur dieser Arbeit bereit erklärt hat.
- Katharina Grosse für die Einweisung in das Experiment, ihre tatkräftige Betreuung und stetige Hilfsbereitschaft.
- Steffen Schüttler, David Steuer und Jan Hendrik Löwer für die vielen unterhaltsamen und aufmunternden Gespräche.
- Meine Familie, die immer für mich da ist und insbesondere meinem Vater Thomas Frings für die vielen Stunden des Korrekturlesens.
- Alle Mitarbeiter und Techniker des Lehrstuhls für die Unterstützung und vielen Ratschläge.

A. Appendix

A.1 Shadowgraphy

A.1.1 Images

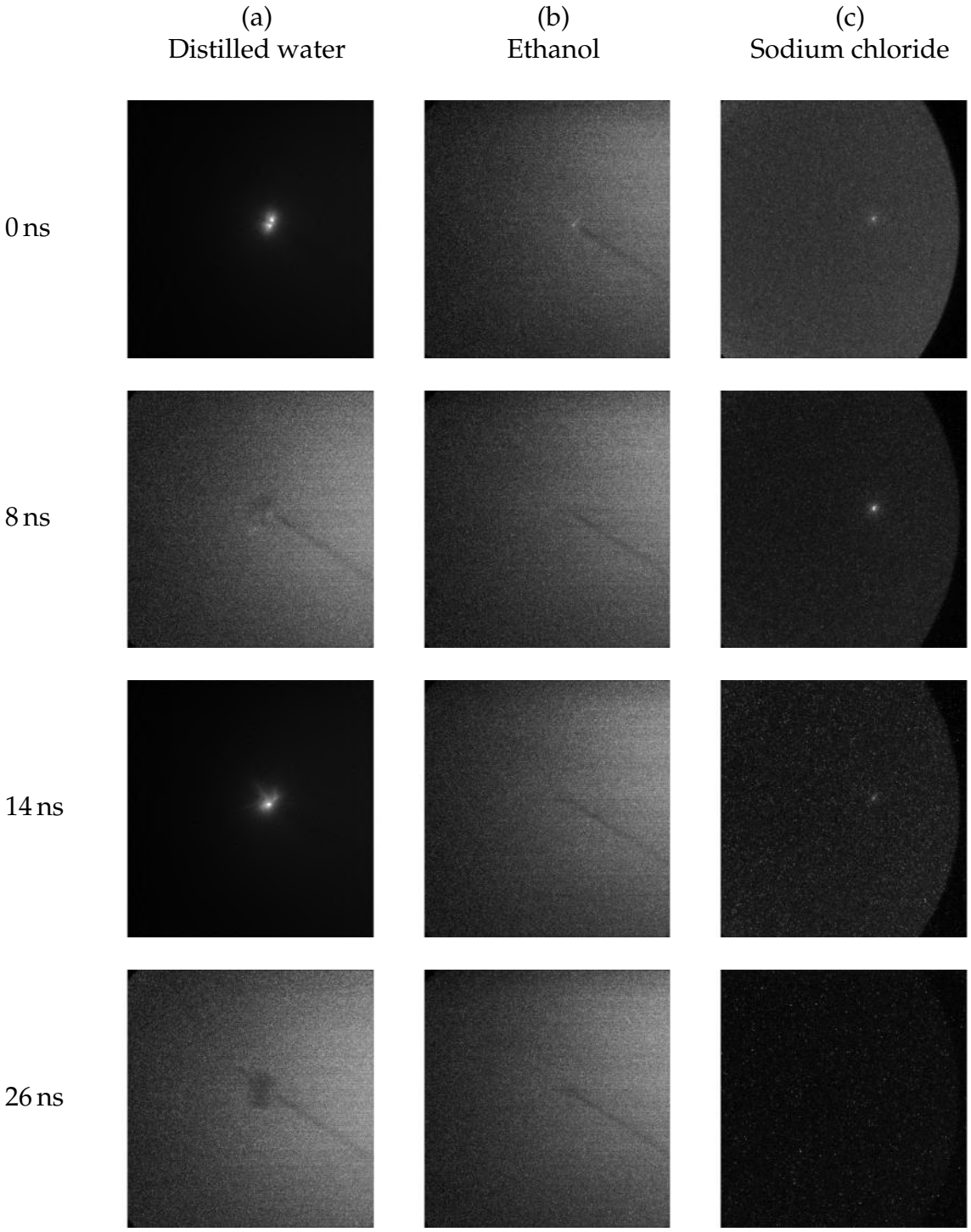

Table A.1: Ignition inside different liquids at four time stages powered at a frequency of 1 Hz. (a) Distilled water: U=2020 kV, t_{gate}=2 ns, gain=255. (b) Ethanol: U=2020 kV, t_{gate}=2 ns, $gain = 255$. (c) Sodium chloride: U=30 kV, t_{gate}=20 µs, $gain = 255$, 100 accumulations.

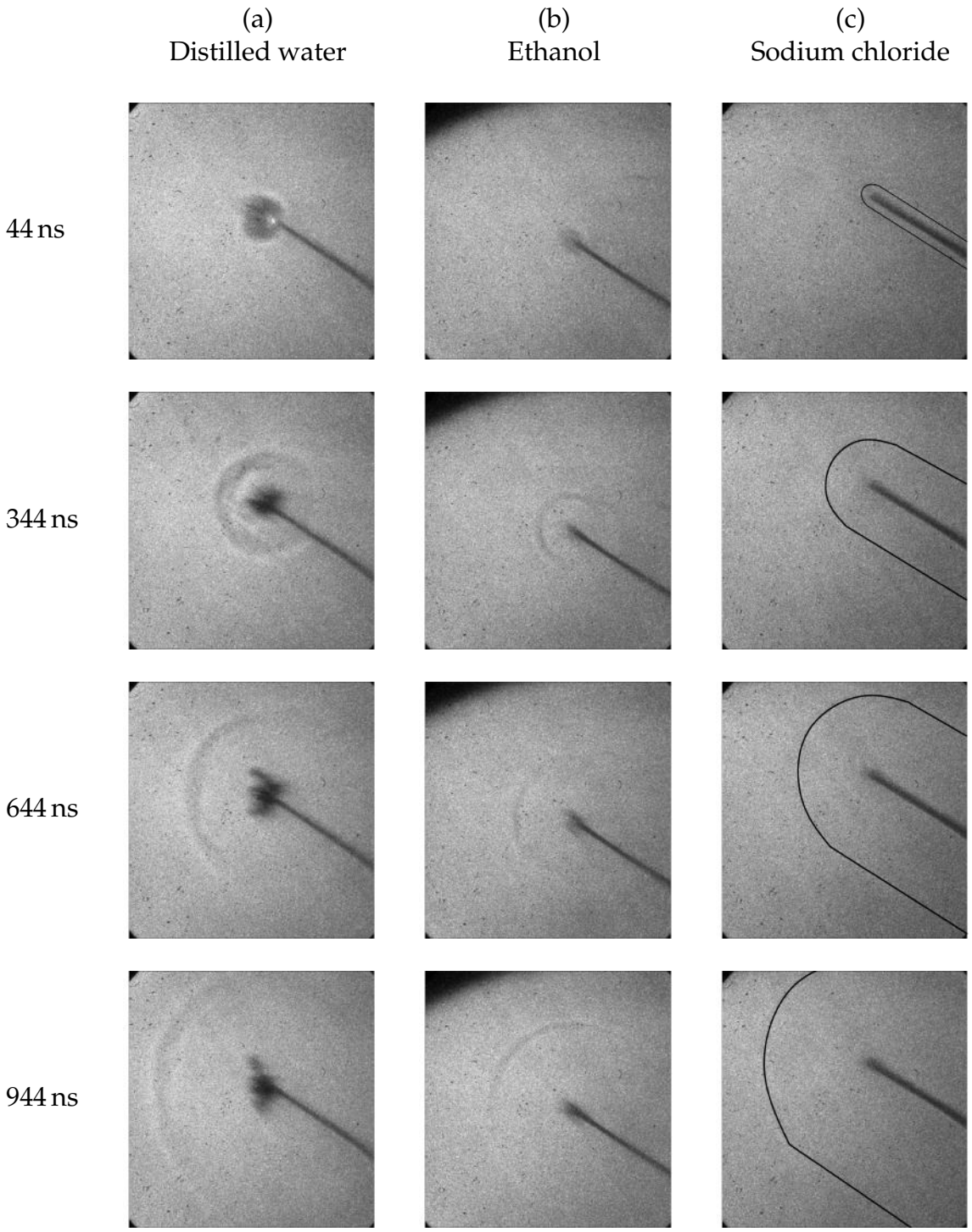

Table A.2: Channel formation inside different liquids at four time stages powered at a frequency of 1 Hz. (a) Distilled water: U=20 kV, t_{gate}=70 ns, gain=255. (b) Ethanol: U=20 kV, t_{gate}=70 ns, gain=255. (c) Sodium chloride: U=30 kV, t_{gate}=70 ns, gain=255.

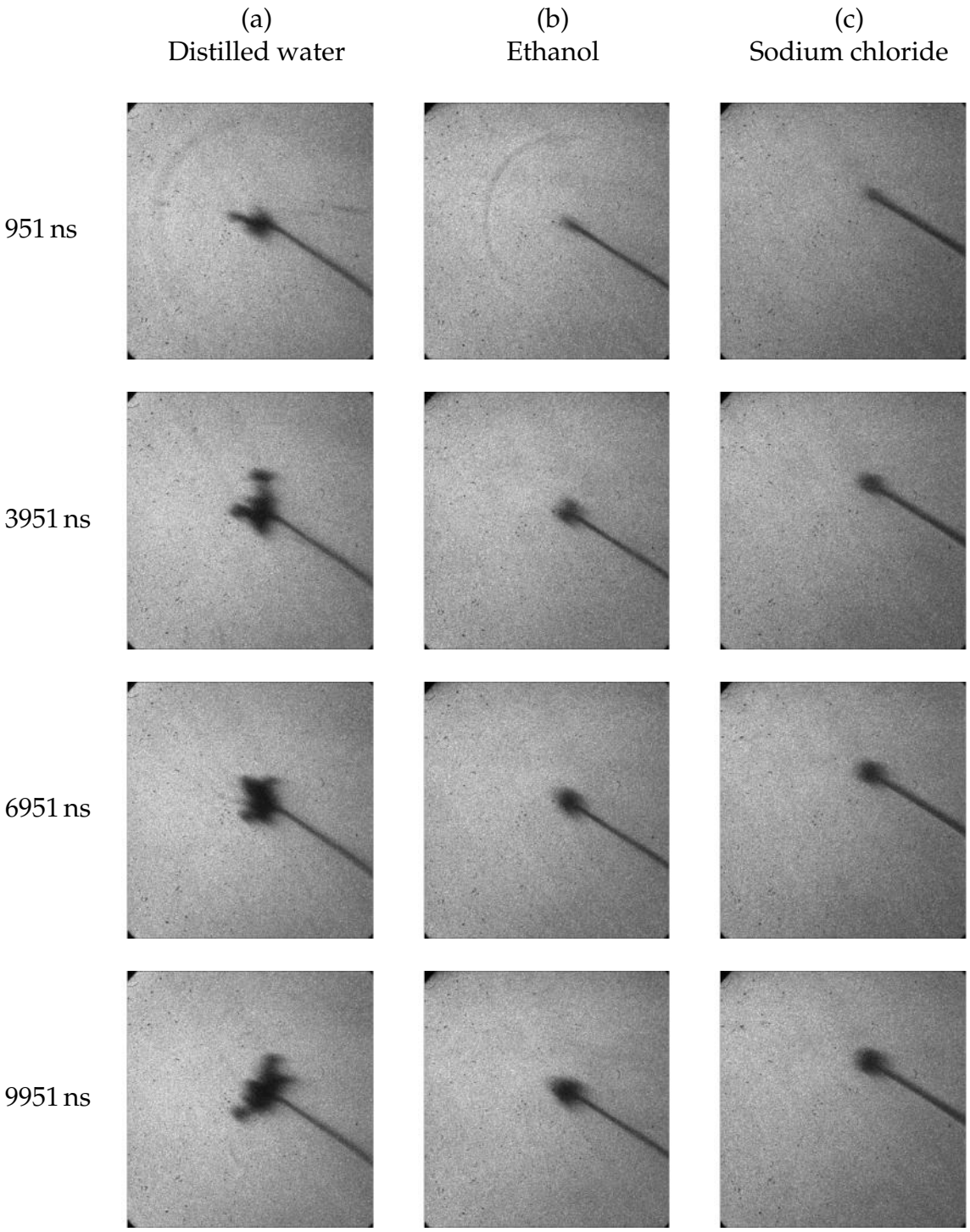

Table A.3: Bubble formation inside different liquids at four time stages powered at a frequency of 1 Hz. (a) Distilled water: U=20 kV, t_{gate}=70 ns, gain=255. (b) Ethanol: U=20 kV, t_{gate}=70 ns, gain=255. (c) Sodium chloride: U=30 kV, t_{gate}=70 ns, gain=255.

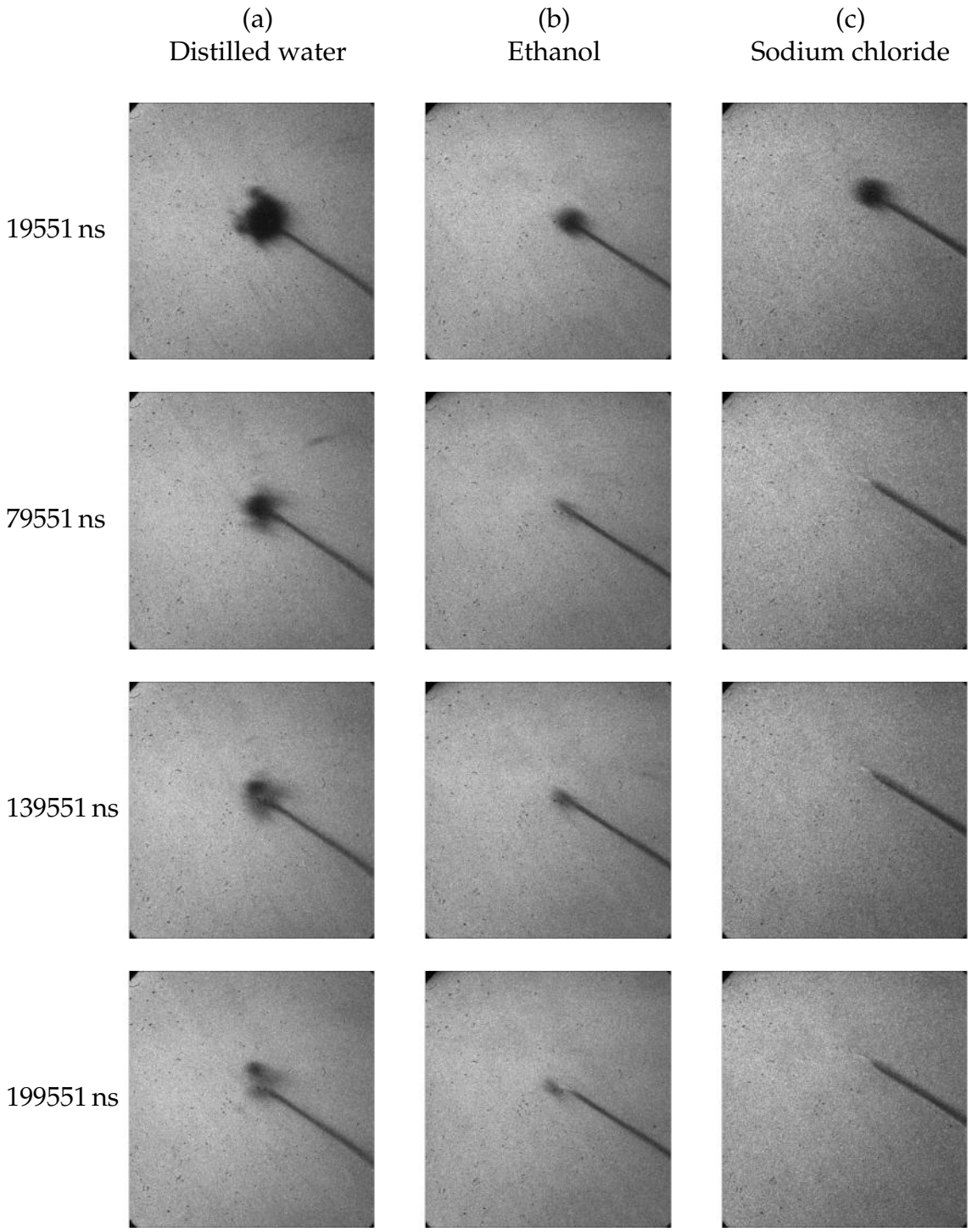

Table A.4: Bubble fade inside different liquids at four time stages powered at a frequency of 1 Hz. (a) Distilled water: U=20 kV, t_{gate}=100 ns, gain=255. (b) Ethanol: U=20 kV, t_{gate}=100 ns, gain=255. (c) Sodium chloride: U=30 kV, t_{gate}=70 ns, gain=255.

A.1.2 Radii of shockwaves

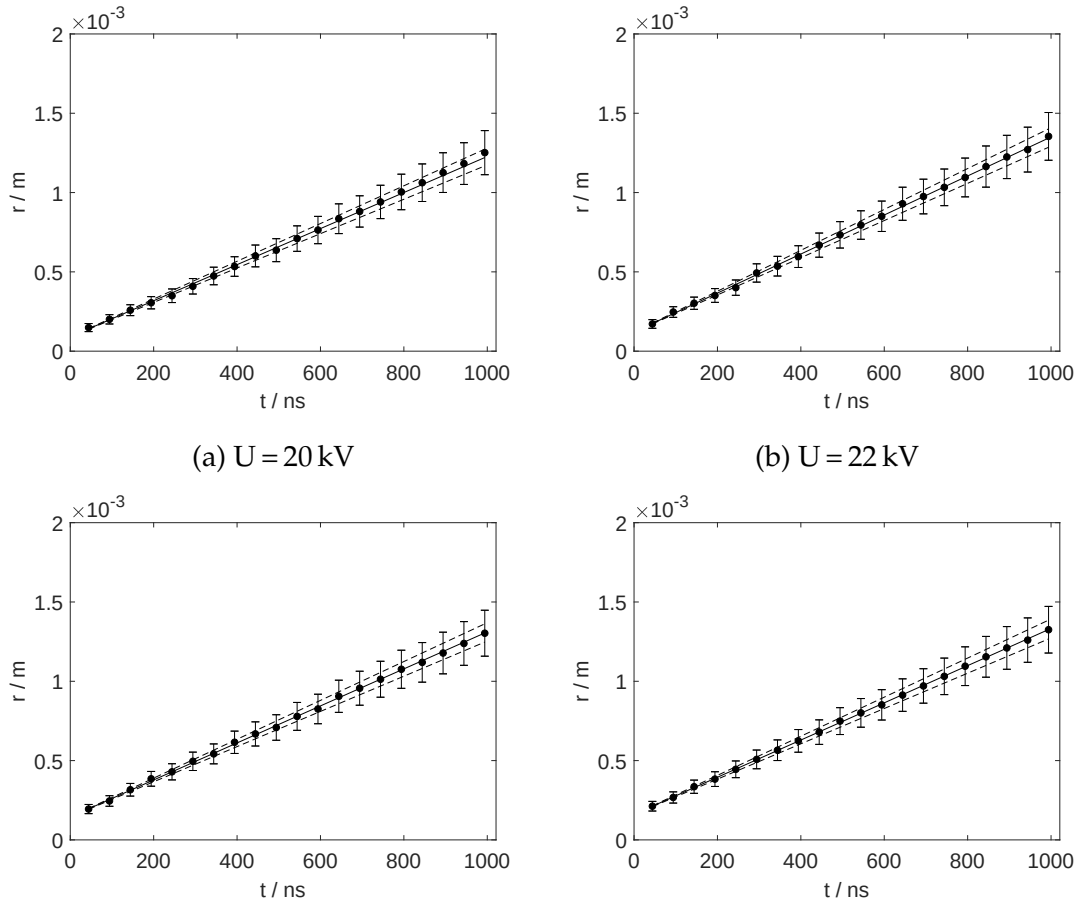

(a) U = 20 kV

(b) U = 22 kV

(c) U = 24 kV

(d) U = 26 kV

Figure A.1.1: Radii of shockwave in ethanol estimated from shadowgraphy at frequency of 1 Hz.

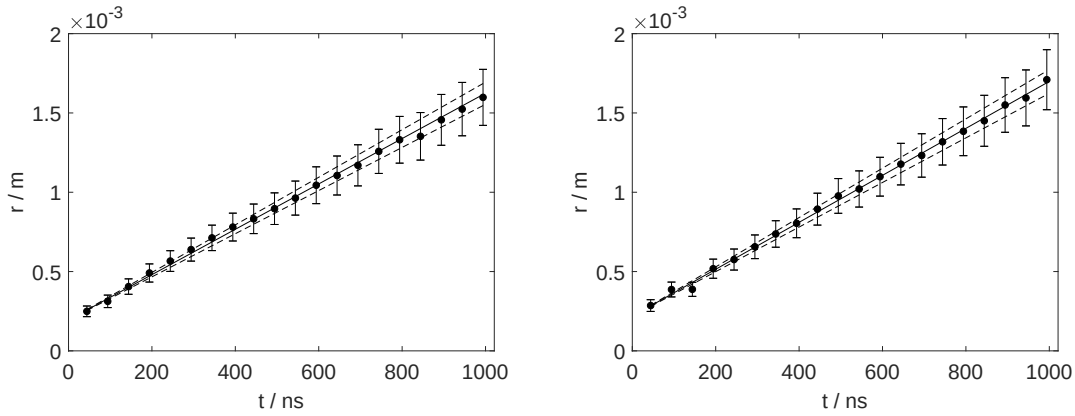

(a) U = 16 kV

(b) U = 18 kV

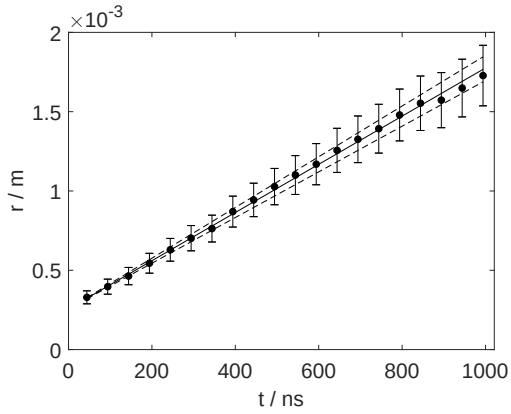

(c) U = 20 kV

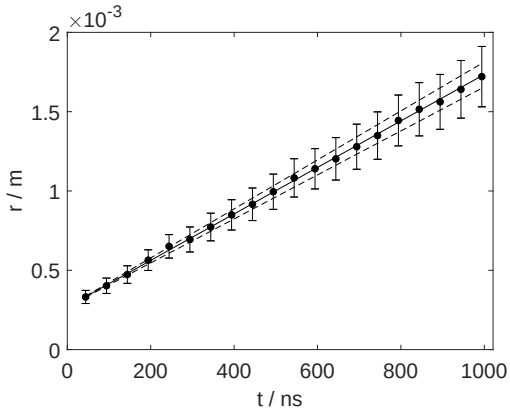

(d) U = 22 kV

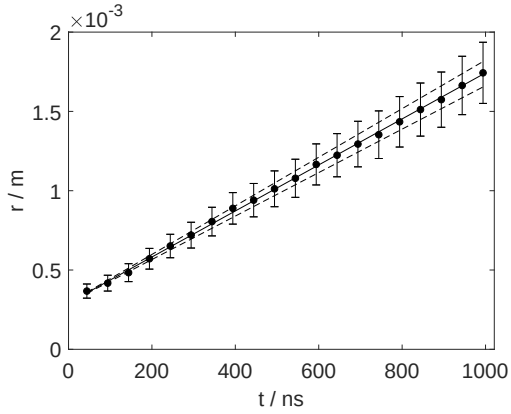

(e) U = 24 kV

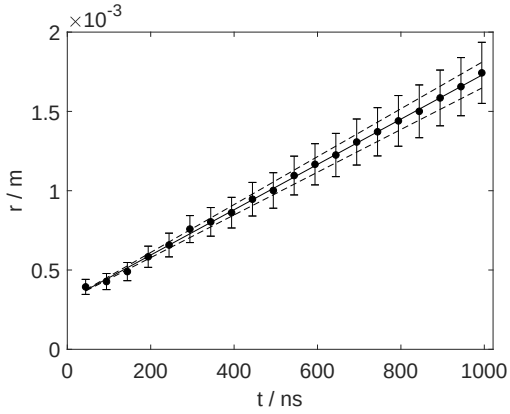

(f) U = 26 kV

Figure A.1.2: Radii of shockwave in water estimated from shadowgraphy at frequency of 1 Hz.

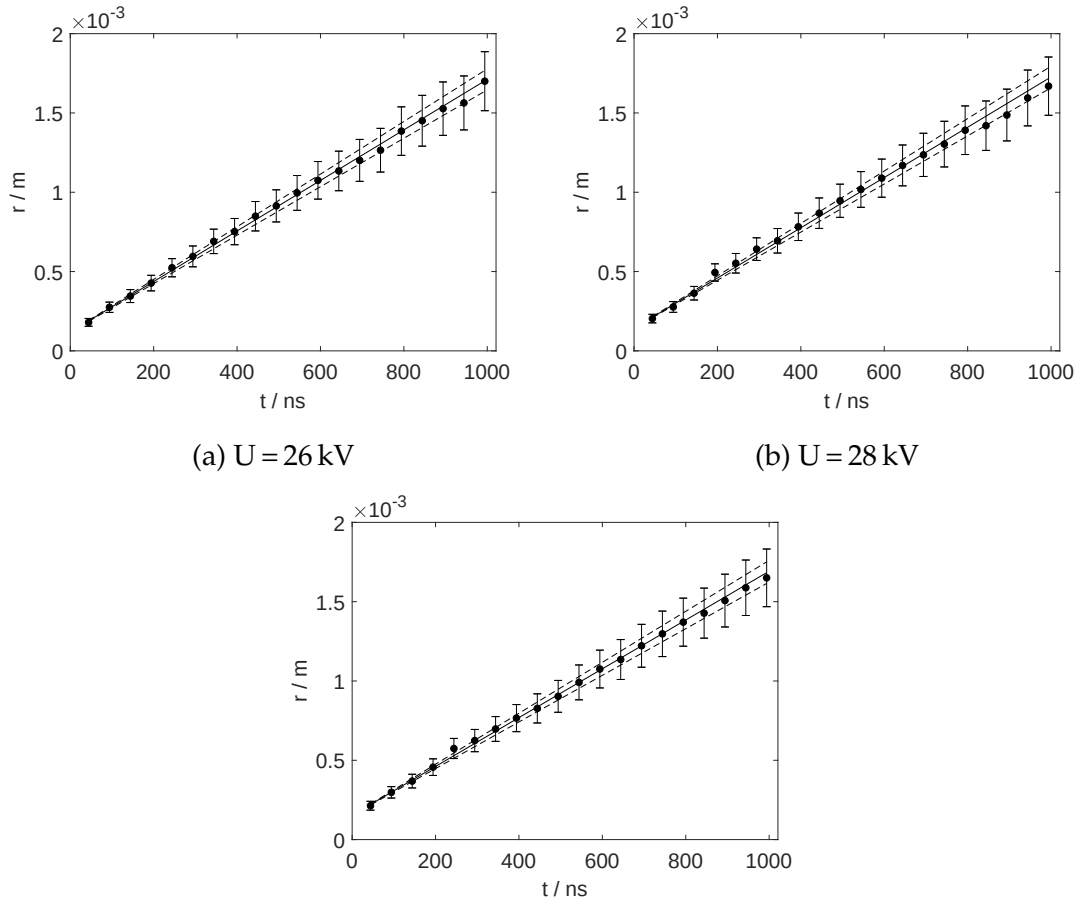

(a) U = 26 kV

(b) U = 28 kV

(c) U = 30 kV

Figure A.1.3: Radii of shockwave in 0.9 % sodium chloride estimated from shadowgraphy at frequency of 1 Hz.

A.2 Schlieren

A.2.1 Images

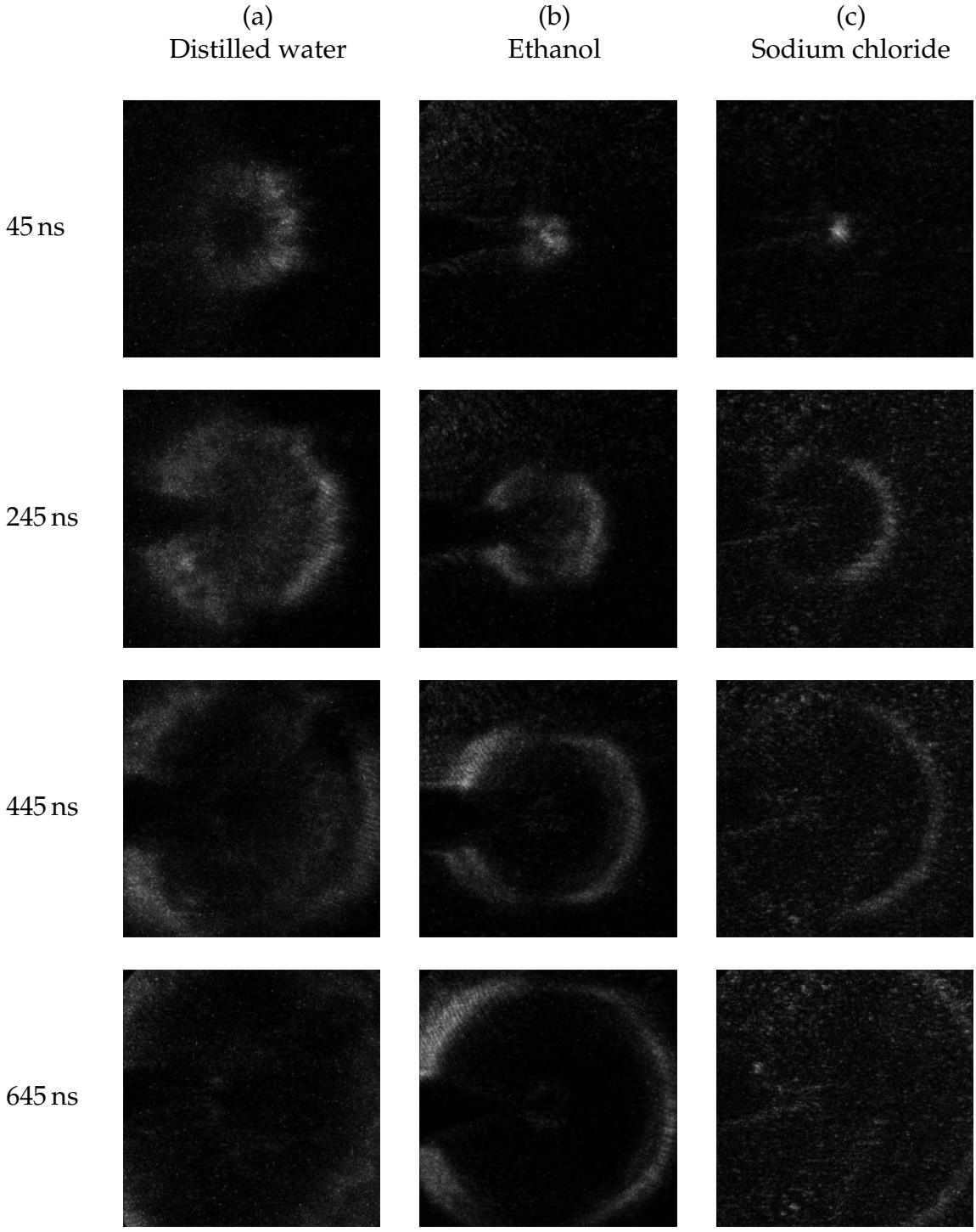

Table A.5: Schlieren images of channel formation inside different liquids at four time stages powered at a frequency of 1 Hz. (a) Distilled water: U=30 kV, t_{gate}=50 ns, gain=255, 20 accumulations. (b) Ethanol: U=30 kV, t_{gate}=50 ns, gain=255, 20 accumulations. (c) Sodium chloride: U=30 kV, t_{gate}=50 ns, gain=255, 20 accumulations.

A.2.2 Radii of shockwaves

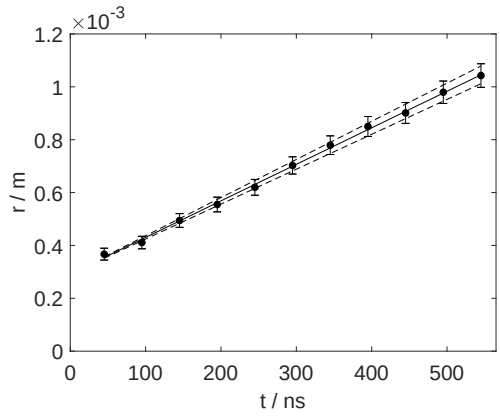

(a) Distilled water.

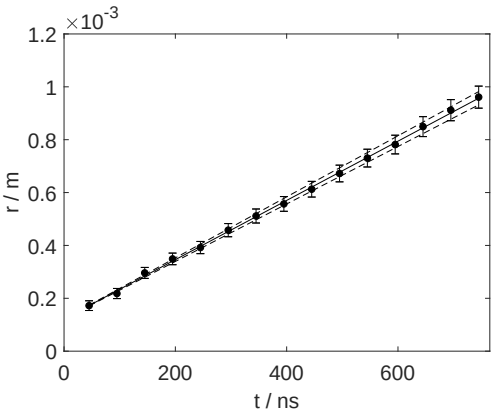

(b) Ethanol.

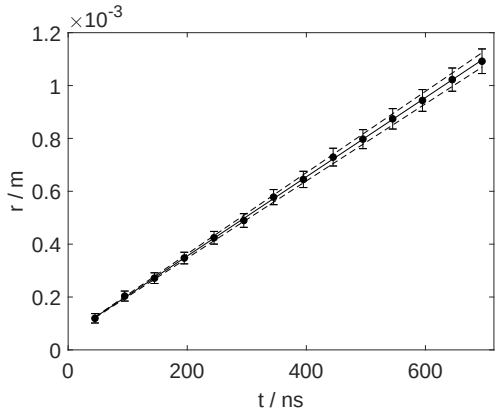

(c) Sodium chloride.

Figure A.2.1: Radii of shockwave estimated from schlieren imaging at 1 Hz and 30 kV.